Energy Conversion and Management: X 24 (2024) 100814

Contents lists available at ScienceDirect

Energy Conversion and Management: X

journal homepage: www.sciencedirect.com/journal/energy-conversion-and-management-x

Blade height impact on self-starting torque for Darrieus vertical axis wind turbines

Hossein Seifi Davari [a,*], Ruxandra Mihaela Botez [b], Mohsen Seify Davari [c], Harun Chowdhury [d], Hasan Hosseinzadeh [e]

[a] Department of Mechanical & Marine Engineering, Chabahar Maritime University, Chabahar, Iran
[b] Laboratory of Applied Research in Active Controls, Avionics, and AeroServoElasticity LARCASE, École de Technologie Supérieure, Université de Québec, Montréal, QC H3C 1K3, Canada
[c] Faculty of Engineering and Technology, Islamic Azad University, Germi, Iran
[d] School of Engineering, RMIT University, Melbourne VIC-3000, Australia
[e] Department of Mathematics, Islamic Azad University Ardabil Branch, Ardabil, Iran

ARTICLE INFO

Keywords:
Embossed-bladed
Darrieus
Power coefficient
Height
Smooth-bladed

ABSTRACT

Self-starting torque ($T_{Self-starting}$) presents a significant challenge for Darrieus vertical axis wind turbines (DVAWTs), often necessitating external assistance to initiate rotation. This study addresses the issue by optimizing airfoil design, employing embossed blades (EBs), and adjusting blade height (H) to reduce $T_{Self-starting}$. From an analysis of 43 rotors at a chord-based Reynolds number (Re_c) of 45,192, national advisory committee for aeronautics (NACA) 0015, NACA4412, and NACA4415 rotors were selected for their superior power coefficients (C_p). These rotors were optimized using double-multiple streamtube theory (DMST) and particle swarm optimization (PSO), focusing on the thickness-to-chord ratio (TCR). Among them, the NACA0015-Opt rotor achieved the highest C_p, demonstrating its effectiveness in enhancing DVAWT efficiency. This study also investigates the effect of H on the performance of EBs, comparing H of 35 cm and 75 cm. Experimental findings reveal that combining airfoil optimization with EBs, along with an increased H, leads to a substantial decrease in $T_{Self-starting}$. Specifically, higher H enhance the aerodynamic performance of EBs by improving airflow over the blade surface, further reducing drag and contributing to a significant reduction in $T_{Self-starting}$. At a H of 75 cm, the embossed blade Darrieus vertical axis wind turbine (EB-DVAWT) equipped with the optimized NACA0015-Opt rotor required 15.92 %, 17.04 %, 18.12 %, 21.23 %, 52.06 %, 49.23 %, 51.25 %, 35.20 %, 14.12 %, and 9.09 % less $T_{Self-starting}$ at wind velocities (U_∞) of 1, 2, 3, 4, 5, 6, 7, 8, 9, and 9.5 m/s, respectively, compared to the baseline smooth blade Darrieus vertical axis wind turbine (SB-DVAWT) with the original NACA0015 rotor.

1. Introduction

For over a century, carbon-based fuels have driven industrial development, but their use has resulted in significant environmental and social challenges. The combustion of fossil fuels releases pollutants like CO_2, NO_x, and SO_2, contributing to global warming and climate change. Extraction processes also cause environmental damage, including habitat destruction and water contamination. Furthermore, dependence on these fuels poses energy security risks due to price fluctuations and geopolitical tensions, emphasizing the urgent need for a shift to renewable energy sources [1–15].

Environmentally sustainable power is defined as energy extracted from natural Procedures that are continuously recharged [16]. This incorporates solar-derived power [17–29], hydropower [30–34], biomass [35–43], geothermal energy [44–48], and wind energy [49–63]. Unlike fossil fuels, renewable energy sources are sustainable, providing a continuous supply of energy with minimal environmental impact. They reduce greenhouse gas emissions, produce little to no pollutants, and contribute to improved air and water quality. Wind and solar energy, both abundant and inexhaustible, enhance energy stability and reduce dependence on non-renewable resources. Among renewable energy solutions, wind power is particularly promising due to its high efficiency in areas with consistent wind patterns and its lower land use compared to solar farms, allowing for dual land use in agriculture [64–79].

Wind energy is captured through wind turbines (WTs), which are

* Corresponding author.
E-mail address: hseifidavary@gmail.com (H. Seifi Davari).

https://doi.org/10.1016/j.ecmx.2024.100814
Received 10 September 2024; Received in revised form 24 November 2024; Accepted 25 November 2024
Available online 28 November 2024

Nomenclature

A	The swept area of the blade (m^2)
C	Chord length (m)
C_D	Drag coefficient (−)
C_L	Lift coefficient (−)
C_p	Power coefficient (−)
C_T	Torque coefficient (−)
D	Rotor diameter (m)
F_D	Drag force (N)
F_L	Lift force (N)
F_N	Normal force (N)
H	Blade height (m)
I	Moment of inertia of the rotor (Kg.m^2)
C_L/C_D	Lift-to-drag ratio (−)
m	Mass of the rotor (Kg)
N	Number of blades (−)
R	Turbine rotor radius (m)
Re_c	Chord-based Reynolds number (−)
S	Solidity of the rotor (−)
T_A	Aerodynamic torque (Nm)
T_D	Aerodynamic drag torque (Nm)
T_f	Frictional torque (Nm)
T_I	Inertia torque (Nm)
T_{Resist}	Resisting Torque (Nm)
$T_{Self-starting}$	Self-starting torque (Nm)
U_∞	Wind velocity (m/s)
α	Angular acceleration (Deg)
β	Angle of attack (Deg)
λ	Tip speed ratio (−)
μ	The coefficient of friction (−)
ρ	Air density (Kg/m^3)
ν	Kinematic viscosity (m^2/s)

Abbreviations

AR	Aspect ratio
CAD	Computer-aided design
CFD	Computational fluid dynamics
DMST	Double-multiple stream tube
DVAWT	Darrieus vertical axis wind turbine
EB	Embossed blade
EB-DVAWT	Embossed blade Darrieus vertical axis wind turbine
gbest	Global best
HAWT	Horizontal axis wind turbine
LWV	Low wind velocity
NACA	National advisory committee for aeronautics
pbest	Personal best
PSO	Particle swarm optimization
SB	Smooth blade
SB-DVAWT	Smooth blade Darrieus vertical axis wind turbine
SMAW	Shielded metal arc welding
SVAWT	Savonius vertical axis wind turbine
TCR	Thickness-to-chord ratio
VAWT	Vertical axis wind turbine
WT	Wind turbine

mainly classified into horizontal axis wind turbines (HAWTs) and vertical axis wind turbines (VAWTs). HAWTs are highly efficient and perform best in areas with consistent wind, but they require a minimum U_∞ and a yaw mechanism for wind alignment, which can reduce efficiency in variable wind conditions. In contrast, VAWTs can operate across a wider range of U_∞, do not require a yaw mechanism, and are better suited for areas with fluctuating wind patterns. Additionally, VAWTs offer advantages such as a lower profile, reduced risk to wildlife, easier installation and maintenance, greater durability, and lower costs compared to HAWTs [80–86].

VAWTs include the Savonius vertical axis wind turbine (SVAWT) and the DVAWT. The SVAWT features a simple drag-based design that allows it to start at low wind velocities (LWVs), but its efficiency is limited, making it unsuitable for large-scale power generation. In contrast, the DVAWT relies on aerodynamic lift, offering higher efficiency and energy output across a wider range of U_∞. However, a significant drawback of the DVAWT is its inability to self-start, requiring an initial push or higher U_∞ to begin operation, which limits its effectiveness in areas with low or variable wind conditions. Despite this, the DVAWT's superior efficiency makes it ideal for large-scale energy generation in regions with consistent wind patterns [87–93].

This study focuses on the DVAWT because of its high efficiency, energy output potential, cost-effectiveness, and ease of construction, all without the need for costly external devices. Although it has a self-starting limitation, the research explores solutions to improve performance in LWV conditions by examining various methods, designs, and strategies to enhance self-starting capabilities and overall efficiency. The goal is to develop more reliable, affordable, and efficient VAWTs for wider applications.

A variable pitch system increased power and torque but also introduced complexity and higher costs, limiting its use in small-scale applications [94,95]. Combining DVAWT with SVAWT boosted the C_p by 26.91 % at low tip speed ratios (λ), but performance declined at higher ratios [96,97]. Increasing the blade chord length (C) enhanced self-starting in Gorlov VAWTs, though it was less effective with thinner airfoils [98]. Helical blade designs improved efficiency but created manufacturing and maintenance challenges, underscoring the trade-off between efficiency and practicality.

Research indicates that flexible plates enhance torque generation in DVAWTs at LWVs [99], but their integration increases manufacturing complexity and costs, limiting their suitability for large-scale applications. J-shaped blades are effective for self-starting in urban LWV conditions [100], but their design and manufacturing complexity pose significant challenges. V-shaped blades perform well under certain conditions but lose efficiency at low λ and are expensive to construct. These issues highlight the need for simpler, more cost-effective designs that maintain or enhance self-starting performance without the complications of advanced systems [101].

The rough surface component, functioning as a passive control method, improves the aerodynamic efficiency of VAWTs by minimizing airflow separation effects [102]. While existing studies on roughness elements and other surface modifications have provided valuable insights into passive control methods for VAWTs, they have limitations that leave room for further exploration. Keskin et al.'s study [103] on roughness elements applied to a DVAWT with NACA0018 blades relied mainly on 2D simulations. While these simulations are useful for initial optimization, they don't account for the complexities of real-world turbine conditions. Additionally, the study only examined roughness at a few chordwise positions (5 %, 10 %, and 50 %) and didn't consider its effect across the full span of the blade, limiting our understanding of how surface modifications impact aerodynamic efficiency and power output in actual operational settings.

Tanürün et al.'s [104] study investigated the impact of suction-side roughness on the aerodynamic performance of the NACA0015 rotor in a VAWT. However, it was limited to applying single- and double-layer roughness only on one side of the blade, which improved the lift coefficient (C_L). The study did not explore how symmetrical roughness, full-span treatments, or varying H might influence self-starting, stall delay, or peak performance at different λ values. Additionally, it did not consider the potential advantages of alternative textures such as embossed patterns.

Other studies, such as those examining sinusoidal leading-edge protrusions, demonstrate that tubercle designs can delay stall and enhance aerodynamic efficiency for specific airfoils. However, these studies primarily focus on isolated airfoil sections in 2D simulations or wind tunnel experiments, rather than full turbine systems [105].

Gonçalves et al. [106] observed performance improvements with leading-edge modifications at specific U_∞, but these effects have not been thoroughly tested in the dynamic rotational environment of a DVAWT, where conditions vary throughout the rotation cycle.

Zamani et al. [107] explored the use of porous media elements in the DU 06-W-200 airfoil, showing benefits in stall delay and improved flow attachment. However, their study was limited to 2D simulations and did not evaluate how these elements would perform on a complete VAWT in fluctuating wind conditions. Additionally, the porous elements were tested only on the pressure and suction sides, limiting understanding of their effectiveness across the entire rotor blade or when combined with other surface modifications like embossing.

The decision to investigate EB surfaces is based on their demonstrated aerodynamic benefits for VAWTs. Previous studies have shown that roughened surfaces can enhance airflow attachment, delaying flow separation and reducing drag at certain angles of attack (β).

EB surfaces, a form of structured surface roughness, presents a promising and innovative solution to enhance the aerodynamic performance of DVAWTs. By introducing textured patterns across the blade surface, these designs improve self-starting capabilities by modifying local airflow patterns, reducing boundary layer separation, and increasing initial torque. These benefits are especially valuable in LWV conditions, typical of urban environments where DVAWTs are commonly deployed.

The adoption of EB surfaces is significant for their ability to balance enhanced aerodynamic performance with manufacturing simplicity. Unlike complex mechanisms such as variable pitch systems, embossed surfaces provide a cost-effective, passive control method suitable for small- and medium-sized VAWTs operating in variable U_∞ conditions. This aligns with recent research advocating passive solutions to optimize blade performance while minimizing manufacturing and operational complexity.

This study builds on these principles by proposing the application of embossed patterns across the full H and surface of the DVAWT blade. Departing from prior studies that restricted roughness modifications to isolated blade sections or specific chordwise positions, this comprehensive approach aims to address both flow separation and self-starting challenges with a uniformly textured surface.

This research investigates full-span embossed patterns to provide a scalable and effective solution for improving aerodynamic efficiency, stall delay, and self-starting performance in real-world conditions. This holistic strategy addresses main gaps in the literature, offering a practical pathway for advancing DVAWT performance and viability in diverse environments.

Building on previous research findings, which highlight the absence of a definitive design condition for airfoil optimization in VAWTs due to their operation across a wide range of positive and negative β [108], this study investigates a diverse set of 43 airfoil designs. These airfoils, drawn from the NACA 4-digit, NACA 5-digit, and Selig families, were systematically analyzed to identify the most suitable candidates for optimizing VAWT performance in this research.

Moreover, as highlighted in studies by Bachant and Wosnik [109] and Miller et al. [110], the performance of DVAWTs is strongly influenced by the Re_c. Our investigation is conducted at a Re_c of 45,192, calculated based on a blade C of 0.071 m, to account for this critical factor. This parameter was selected to reflect the operational conditions relevant to the design and performance evaluation in this study.

Research has demonstrated that incrementing the aspect ratio (AR)—defined as the ratio of H to the diameter (D) of the DVAWT—enhances the blade's surface area exposed to airflow, thereby improving the C_p [111,112]. This effect is particularly pronounced in SB-DVAWTs, where higher AR values maximize air contact area and directly improve aerodynamic efficiency. Building on this finding, this study investigates AR as a critical factor influencing turbine performance, with a specific focus on its impact on $T_{Self-starting}$. To further explore this relationship, we examine the effects of blade embossment in combination with increased H. Unlike previous studies that primarily focused on H in SB configurations, our approach includes a comparative analysis of traditional SBs and EBs to assess their combined influence on the self-starting performance of DVAWTs.

For this study, we consider two AR values: 1 and 2.4, representing key practical ranges for DVAWT applications. $AR = 1$ is commonly used for compact, small-scale DVAWTs, particularly in urban environments where space constraints prioritize efficiency over peak power output. Conversely, $AR = 2.4$ is often selected in DVAWT research for its balance between efficiency, structural feasibility, and operational stability, offering increased rotor inertia and reduced tip flow effects [112,113].

Increasing the AR from 1 to 2.4 will enhance DVAWT performance significantly. In the sub-8 AR range, tip flow effects are sensitive to changes in AR. As noted by Tong et al. [114], increasing AR reduces tip flow interference, which improves both aerodynamic efficiency and overall performance. By raising the AR to 2.4, the DVAWT exposes a larger blade area to the wind while maintaining manageable design complexity and cost. This adjustment aligns with findings demonstrating its potential to improve the C_p and self-starting capabilities.

We carefully chose these AR values to encompass a range of operational scenarios commonly encountered in VAWT research. $AR = 1$ represents compact, urban-focused designs, while $AR = 2.4$ provides a benchmark for enhanced efficiency in larger systems. By evaluating these two AR values, this study seeks to address gaps in the literature by exploring how blade embossment interacts with H to influence $T_{Self-starting}$. This area has received limited attention in previous research. This comprehensive analysis aims to provide insights into optimizing DVAWT performance through practical and innovative design strategies.

Researchers have made various efforts to enhance the performance and self-starting functions of DVAWTs, as extensively documented in the literature. These initiatives seek to address the inherent challenges of DVAWT design and improve overall performance. However, a notable gap exists regarding the comparative analysis of EB designs and the optimization of airfoil geometry, particularly concerning the TCR, for enhancing $T_{Self-starting}$.

Furthermore, researchers have not comprehensively studied the combined influence of EB geometry, airfoil optimization, and H. This study seeks to fill these gaps by investigating how variations in H, when paired with EB designs and optimized airfoil geometry, affect the $T_{Self-starting}$ of DVAWTs. Moreover, this research aims to identify simple and cost-effective methods to improve DVAWT self-starting capabilities without relying on external devices or complex airfoil structures. By focusing on practicality and affordability, the study emphasizes designs that reduce construction complexity and manufacturing costs. This approach is particularly valuable for developing DVAWT, where simplicity in design can facilitate broader adoption, especially in small-scale or urban applications.

Researchers have employed various experimental [115–117] and computational models, including computational fluid dynamics (CFD) [118–120] and momentum models like streamtube models, to assess VAWT efficiency. The DMST model stands out for its speed and accuracy, consistently aligning with experimental data and CFD simulations [121–125]. Its reliability has been validated through extensive testing, and several refinements have enhanced its accuracy [126–128], particularly for low and moderate solidity (S) VAWTs and variable-pitch designs [127–130].

For a high S turbine, Ghiasi et al. [131] conducted a validation research using a developed DMST model, comparing its predictions with experimental data provided by Elkhoury et al. [132]. The turbine analyzed in their study was a micro-scale, H-type, three-bladed DVAWT characterized by high S ($S = 0.75$), with a $H = 0.8$ m and a D of 0.8 m. The turbine featured a symmetrical NACA0018 blade profile with a C of 0.2 m. The turbine's performance was validated by assessing the C_p over a λ range of 0–3. Their results demonstrated a strong correlation between the experimental C_p at a U_∞ of 8 m/s and the predictions generated by the DMST model, confirming the model's accuracy. Assuming constant U_∞, frontal area, and airflow density, the relationship between C_p and λ remained consistent across experimental and simulation datasets. The maximum observed discrepancy occurred at $\lambda = 1$, with a deviation of 8 %. Building upon the established reliability of advanced DMST codes, this study also employs a developed DMST code for numerical simulations.

Also, researchers generally consider high-S turbines to have superior self-starting capabilities compared to their low-S or moderate-S counterparts. This advantage is primarily attributed to their higher average static torque coefficient (C_T), which enhances the turbine's ability to initiate rotation under LWV conditions [133,134]. Additionally, high S turbines demonstrate improved C_p at lower λ, enabling them to operate efficiently at reduced rotational speeds. This characteristic not only improves performance at lower U_∞ but also minimizes the generation of excessive centrifugal forces, thus reducing the structural strength requirements for the turbines [135].

Considering that the primary objective of this study is to improve self-starting capabilities, we have selected an S value of 0.608. This high S configuration strikes an optimal balance between efficient self-starting characteristics and operational efficiency at lower λ. By choosing this S value, we expect the turbine to exhibit enhanced static torque and maintain performance at lower U_∞, which aligns with the goals of improving the self-starting behavior without introducing excessive mechanical stresses [123]. This selection of S of 0.608, is consistent with the findings of Ghiasi et al. [131], who validated high S turbines using developed DMST models and confirmed their superior performance under similar design configurations. Thus, the choice of $S = 0.608$ is grounded in both theoretical advantages and empirical evidence, demonstrating that the turbine operates with enhanced self-starting capabilities. This choice minimizes structural challenges and maximizes efficiency at lower rotational speeds.

2. The DMST model

Paraschivoiu [136] developed the DMST model, which divides the rotor area into upwind and downwind regions to simulate airflow through actuator disks (Fig. 1) [137]. The model combines two key theories: momentum theory, which analyzes aerodynamic forces using momentum conservation, and blade element theory, which assesses the forces on individual blade sections based on geometry and aerodynamics. This combined approach allows the DMST model to accurately simulate turbine performance under various operational conditions.

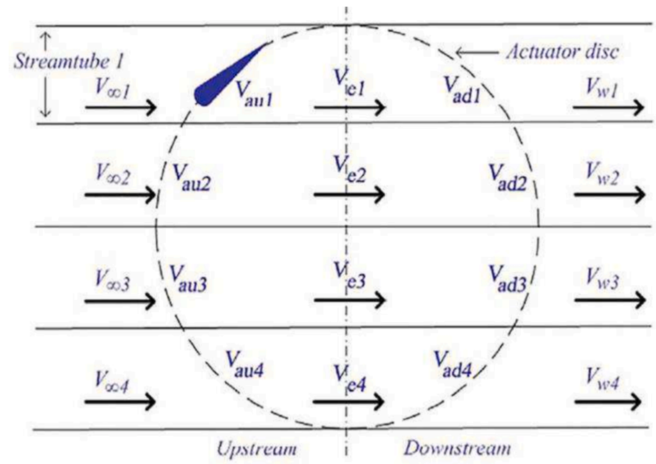

Fig. 1. DMST model diagram by Batista et al. [137].

In the DMST methodology, instead of dividing the rotor blade into fixed sections, the rotor's perimeter is divided into a finite number of stream tubes. This approach, explained by Islam et al. [138] and Paraschivoiu [129], is illustrated in a new DMST code, as shown in the flowchart (Fig. 2). The process begins with defining the geometric parameters of the DVAWT, such as C, D, and blade configuration. Next, the rotor is divided into upwind and downwind areas.

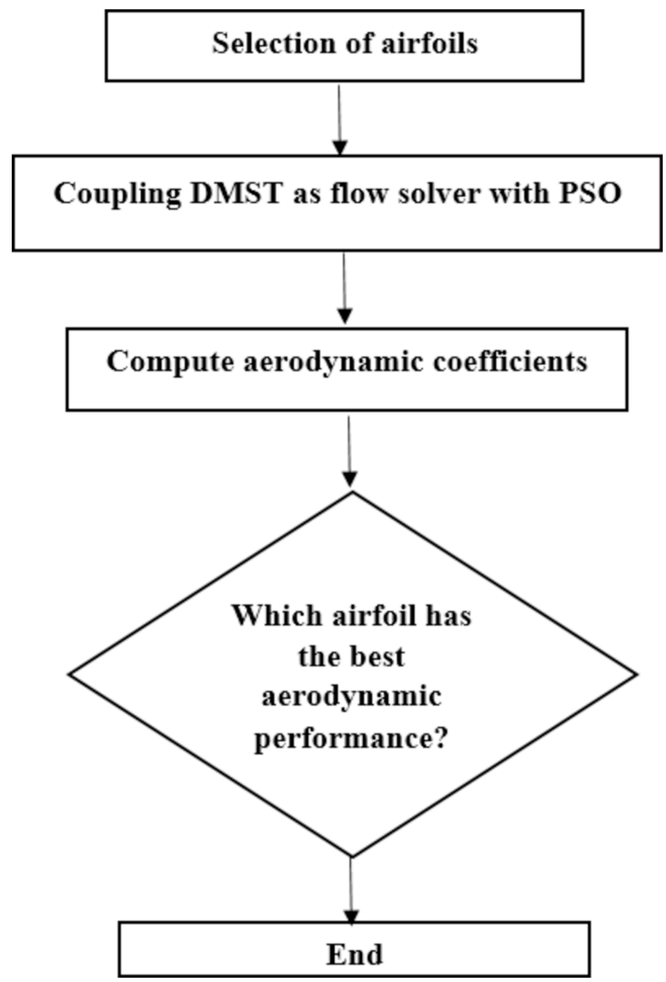

Fig. 2. Developed flowchart of DMST.

To validate the effectiveness of the MATLAB code, we compared the data with experimental data from Sheldahl et al. [139], obtained at the Sandia Wind Tunnel Laboratories. The VAWT used in the experiments had a H of 5.10 m, a C of 0.1524 m, and we equipped it with a NACA0015 airfoil.

The Re_c was 330,000, and the standard deviation S was 0.129. Additionally, we compared the MATLAB code results with the model presented by Paraschivoiu [129] for further validation. The comparison, presented in Fig. 3, depicts a close correlation between the simulated data and the wind tunnel data [129,139], thus confirming the validity of the MATLAB code and its implementation. However, to more rigorously

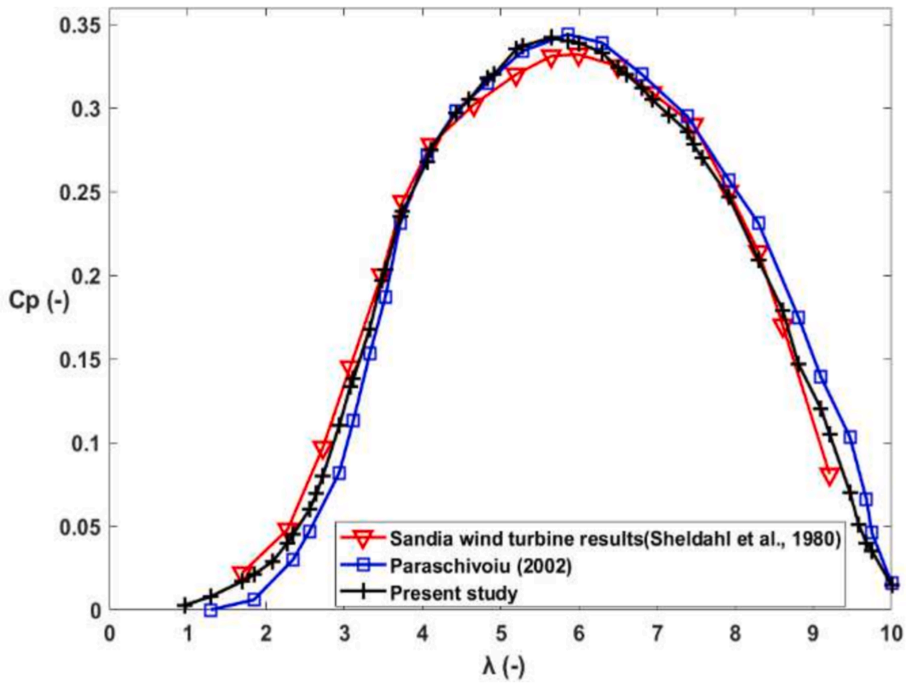

Fig. 3. Wind tunnel and DMST model data.

assess the accuracy of the predictions, we conducted an uncertainty analysis by calculating the relative uncertainty between the predicted and experimental C_p values at each corresponding λ.

The calculated relative uncertainties for all λ—namely, 1.30, 1.85, 2.35, 2.56, 2.94, 3.12, 3.33, 3.53, 3.72, 4.06, 4.43, 4.83, 5.28, 5.86, 6.30, 6.81, 7.39, 7.92, 8.30, 8.81, 9.10, 9.47, 9.68, 9.75, and 10—are as follows: 28 %, 25 %, 20 %, 17 %, 16 %, 12 %, 9.8 %, 8.55 %, 1.73 %, 1.47 %, 0.34 %, 0.95 %, 0.90 %, 1.16 %, 1.77 %, 2.5 %, 3.05 %, 3.89 %, 9.52 %, 16 %, 13.68 %, 28 %, 25 %, 23.91 %, and 6.25 %, respectively. The mean relative uncertainty across all data points is 11.06 %, based on experimental data from Paraschivoiu [129]. This suggests that while the model generally shows minimal discrepancy, specific λ values exhibit higher uncertainty. Notably, the maximum deviations of 28 % occur at λ values of 1.30 and 9.47, while we observe the minimum deviation of 0.34 % at $\lambda = 4.43$. The model performs more accurately at lower λ values, likely due to the more predictable flow conditions at these operating points.

In contrast, we attribute the higher uncertainties observed at both low ($\lambda = 1.30$) and high ($\lambda = 9.47$) λ values to more complex flow phenomena, such as flow detachment and increased vortex shedding, which are difficult to model with high precision. The calculated relative uncertainties for all λ—namely, 1.7, 2.28, 2.73, 3.08, 3.48, 3.75, 4.11, 4.66, 5.20, 5.65, 6, 6.5, 6.94, 7.47, 7.92, 8.3, 8.61, and 9.21—are as follows: 22.73 %, 16.67 %, 17.53 %, 8.28 %, 1.50 %, 2.46 %, 1.08 %, 0.99 %, 4.69 %, 3.32 %, 2.11 %, 0.31 %, 1.29 %, 4.14 %, 1.20 %, 2.34 %, 5.29 %, and 29.63 %, respectively. The mean relative uncertainty across all data points is 6.97 %, based on experimental data from Sheldahl et al. [139].

These results indicate that the discrepancy between the predicted and experimental values is generally small, and the model performs better at lower λ values. Notably, the maximum deviation of 29.63 % occurred at $\lambda = 9.21$, while the minimum deviation of 0.31 % occurred at $\lambda = 6.50$. The model exhibits greater discrepancies at higher λ values and performs more accurately at lower λ values, where the flow conditions tend to be more stable.

The deviations observed between the MATLAB predictions and experimental data result from a range of aerodynamic and computational factors. We commonly encounter these discrepancies in WT simulations, and we can explain them as follows:

1. Aerodynamic phenomena at higher λ

At higher λ, the flow around DVAWT blades becomes more complex due to increased rotational speeds, leading to flow separation, tip losses, and vortex shedding, which are challenging to model accurately with simplified aerodynamic models. The DMST model, while efficient, relies on several assumptions that may introduce errors in areas with more complex flow. These assumptions include axisymmetric flow, which overlooks yaw misalignment or blade pitch variations, and steady-state flow, even though real-world conditions may involve instability, especially at higher λ or in turbulent winds.

2. Wind tunnel testing and experimental limitations

The experimental data for validation were obtained in a wind tunnel, but several limitations may cause discrepancies:

Scale effects: Wind tunnel tests often use scaled-down models, which may not fully replicate the aerodynamic behavior of full-scale DVAWTs, leading to differences due to Re_c effects and scaling laws.

Environmental factors: Although wind tunnel conditions are controlled, real-world factors like wind gusts, turbulence, and varying U_∞ can cause deviations between experimental and theoretical results.

3. Measurement accuracy and data uncertainty

Uncertainty in experimental measurements can also contribute to discrepancies between the predicted and experimental data. The uncertainty in the measurement of the C_p and λ may arise from the following factors:

Instrument Precision: The accuracy of the sensors and data acquisition system used to measure parameters such as the C_p and rotational speed can introduce minor errors in the experimental data.

Data Processing: The methods employed to extract the C_p from experimental data may introduce minor inaccuracies, particularly during post-processing, where researchers might use filtering or smoothing techniques to address noise.

4. Re_c Effects

The Re_c significantly influences the determination of the flow characteristics over the VAWT blades. In the experimental setup, the Re_c was 330,000, which may differ from the values encountered in full-scale operations. Consequently, discrepancies between the MATLAB simulation and the experimental results may arise due to Re_c effects, as the turbulence behavior changes with Re_c, especially at higher λ values where the flow is more sensitive to these changes.

3. Airfoil properties

In this study, we evaluated the maximum C_p value of 43 DVAWT rotors, which included symmetrical and unsymmetrical NACA 4-digit, 6-digit, and Selig airfoils, at a $Re_c = 45{,}192$ utilizing the DMST model developed in this work. The selection of symmetrical and unsymmetrical airfoils was motivated by the need to explore a broader range of aerodynamic characteristics and ensure a comprehensive assessment of their performance at the specified Re_c of 45,192. This approach aimed to validate the behavior and efficiency of various airfoil types under identical flow conditions, thereby enabling an accurate comparison and understanding of their aerodynamic performance at this specific Re_c. While the superior performance of symmetrical airfoils in VAWT applications is well-documented, including unsymmetrical airfoils provided an opportunity to investigate potential improvements in lift generation and operational efficiency under these specific flow conditions.

The density (ρ) and kinematic viscosity of the air (v) were 1.19 kg/m^3 and 0.00001571 m^2/s, respectively. The C was 0.071 m, and the inlet U_∞ was set at 10 m/s. We calculated the Re_c using Eq. (1). The selection of the airfoils relied on a combination of aerodynamic efficiency, the availability of reliable data, and their relevance to current VAWT designs in the field. NACA 4-digit and 6-digit airfoils were chosen for their well-documented aerodynamic properties. In contrast, we included Selig airfoils to evaluate the performance of modern airfoils specifically designed for LWV applications, such as those encountered in VAWTs.

$$\mathrm{Re}_c = \frac{U_\infty C}{v} \tag{1}$$

Table 1 presents the peak C_p values obtained for all turbines analyzed at aRe_c = 45,192. Among the 43 airfoils analyzed, the NACA0015, NACA4412, and NACA4415 exhibited the highest C_p within the λ range of 0 to 3. Specifically, the NACA0015 achieved a peak$C_p = 0.1550$ at a λ = 2.50. The NACA4412 reached a peak$C_p = 0.1563$, and the NACA4415 attained a maximum$C_p = 0.1605$ at a λ = 1.50. Due to their superior performance within the tested λ range, we selected these three airfoils for further investigation and potential shape modification.

Table 1
The peak C_P values for all turbines at a Re = 45,192.

Airfoils	λ	Maximum C_P
NACA0015	2	0.155
NACA0016	2	0.148
NACA0018	2	0.125
NACA0022	2	−0.010
NACA0025	2	0.139
NACA0030	2	−0.09
NACA0035	2	−0.15
NACA3519	2	0.014
NACA3521	2	0.029
NACA3522	2	0.0388
NACA3523	2	−0.083
NACA3524	2	−0.097
NACA4412	2.50	0.1563
NACA4415	1.50	0.1605
NACA6515	2	0.147
NACA6520	2	0.056
NACA6521	2	0.127
NACA6530	2	−0.112
NACA63(3)-618	2	−0.0319
NACA63(4)-221	2	−0.019
NACA63(4)-421	2.50	0.105
NACA64(1)-112	2	0.104
NACA64(2)-215	2	0.087
NACA64(3)-218	2	0.105
NACA64(4)-221	2.50	0.087
NACA64(4)-421	2.50	0.0865
NACA65(3)-218	2	0.037
NACA65(4)-221	2.5	0.0426
NACA65(4)-421	2.50	0.0262
NACA66(1)-212	2	0.098
NACA66(2)-215	2	0.0667
NACA66(2)-415	2	0.0663
NACA66(3)-218	2	0.0380
NACA66(4)-221	2	0.0120
S814	2.5	0.047
S815	2	−0.087
S818	2	−0.300
S821	2	0.0732
S823	2	0.007
S827	2	0.108
S828	2	0.124
S1020	2	0.105
S1046	2	0.089

3.1. Optimization of the NACA0015, NACA4412, and NACA4415 rotors for maximum C_p using PSO algorithm

In this study, the key design variables selected for optimization were the thickness and TCR at critical C locations (e.g., 10 %, 30 %, 50 %, and 80 % of the C). We meticulously adjusted these parameters to enhance the aerodynamic performance of the NACA0015, NACA4412, and NACA4415 rotors at a Re_c of 45,192, to maximize the C_p across various λ.

The NACA0015 featured a maximum thickness of 15.00 % at 29.10 % of the C with zero camber. The NACA4412 airfoil had a maximum thickness of 12.00 % at 29.10 % of the C and a maximum camber of 4.00 % at 39.50 %. Additionally, the NACA4415 airfoil has a maximum thickness of 15.00 % at 29.10 % of the C, and a maximum camber of 4.00 % at 39.50 % of the C.

The optimization process was designed to refine these geometrical parameters, with the goal of enhancing the aerodynamic efficiency of the airfoils. The method for developing the optimized airfoils is depicted in Fig. 4. As shown in Fig. 5, the shape of the NACA0015 airfoil was modified to achieve a maximum thickness of 15.63 % at 28.60 % of the C, and a thickness of 0.56 % at 13.50 % of the C, resulting in the NACA0015-Opt airfoil. The main distinctions between the airfoils of the original NACA0015 and the optimized NACA0015-Opt lie in their thickness distribution and the geometrical characteristics along the C.

Similarly, the shape of the NACA4412 airfoil was modified to attain a maximum thickness of 11.86 % at 31.60 % of the C and a thickness of 4.81 % at 40.10 % of the C, resulting in the NACA4412-Opt airfoil. Furthermore, the NACA4415 airfoil shape was modified to reach a maximum thickness of 13.90 % at 27.80 % of the C and a thickness of 3.88 % at 36.40 % of the C, resulting in the NACA4415-Opt airfoil. These modifications enhanced the airflow characteristics around the three airfoils, improving aerodynamic efficiency under specific operational conditions.

The aerodynamic performance of the modified airfoils, represented by the C_p, was analyzed at a Re_c of 45,192. We conducted investigations for viscous flow at this Re_c, and for λ values ranging from 0 to 3. Fig. 4 illustrates the algorithm used to develop the modified airfoils. The PSO algorithm simulates the social behavior of particles (analogous to birds flocking or fish schooling), where every particle corresponds to a potential answer within the optimization space. In the context of airfoil optimization, each particle corresponds to a specific configuration of the airfoil geometry, characterized by the TCR. The algorithm operates as

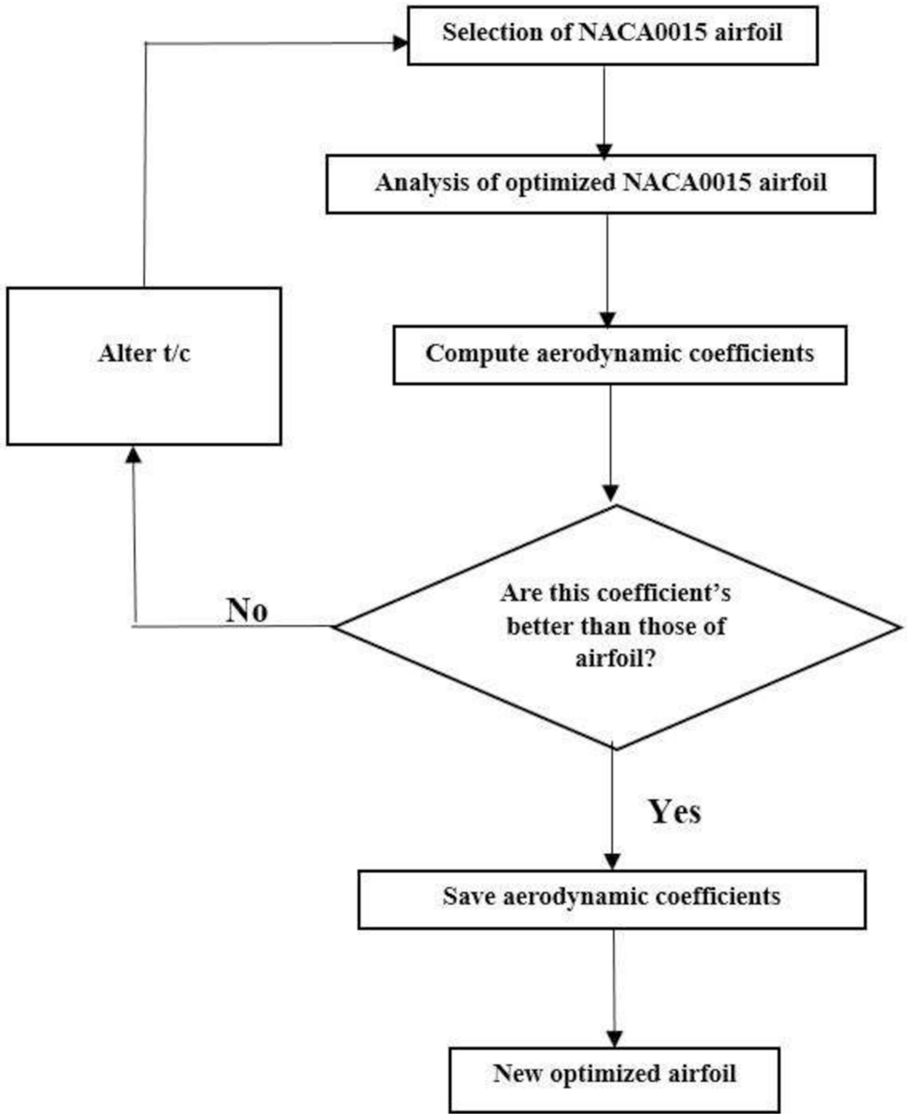

Fig. 4. Flowchart for developing novel airfoil.

follows:

1. Initialization: A swarm of particles is initialized, with each particle assigned a random position and velocity within the parameter space (i.e., the space of airfoil geometries). Each particle represents a distinct airfoil configuration, with its position indicating specific values of thickness and TCR at designated C positions
2. Evaluation: The position of each particle is evaluated based on a predefined objective function that quantifies the aerodynamic performance of the airfoil, such as maximizing the C_p or minimizing drag coefficient (C_D). In this study, the objective function was designed to maximize aerodynamic efficiency, based on a Re_c of 45,192.
3. Particle update: Each particle updates its position and velocity based on two key factors

– Personal best (pbest): This represents the best airfoil geometry encountered by the particle so far.

For each particle, pbest represents the thickness and TCR configuration that resulted in the highest C_p from previous evaluations.

This information guides the particle's movement toward better solutions.

– Global best (gbest): This refers to the best airfoil geometry discovered by any particle in the swarm. The gbest corresponds to the airfoil configuration that has produced the highest overall C_p across all particles in the optimization process. It serves as a benchmark for the entire swarm, guiding particles toward the optimal solutions. Each particle updates its position (airfoil geometry) and velocity (the rate of change of design parameters, such as thickness and TCR) based on the differences between its current position and pbest, as well as the optimal position identified by the entire swarm (gbest).

This update mechanism enables the particles to analyze novel regions of the design space while exploiting known reasonable solutions, thus maintaining a balance between exploration and exploitation. Mathematically, we express the velocity update as:

$$v_i(t+1) = w.v_i(t) + c_1.r_i.(pbest_i - x_i(t)) + c_2.r_2.(gbest - x_i(t)) \tag{2}$$

Where v_i (t + 1) represents the updated speed of particle i at iteration t + 1, v_i (t) is the existing velocity of particle i, w is the inertia weight, which governs the influence of the prior speed, c_1, and c_2 are acceleration coefficients, r_1, and r_2 are random values between 0 and 1, introducing stochastic behavior. $pbest_i$ represents the personal best position of particle i, x_i (t) represents the current position (geometry of the airfoil), and $gbest$ is the global best location identified by any particle.

The updated position x_i (t + 1) represents the new airfoil geometry,

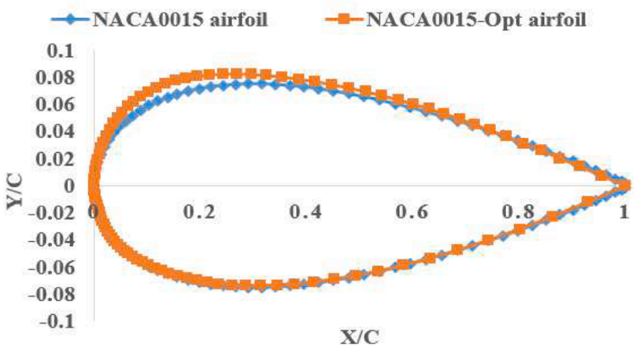

(a) NACA0015

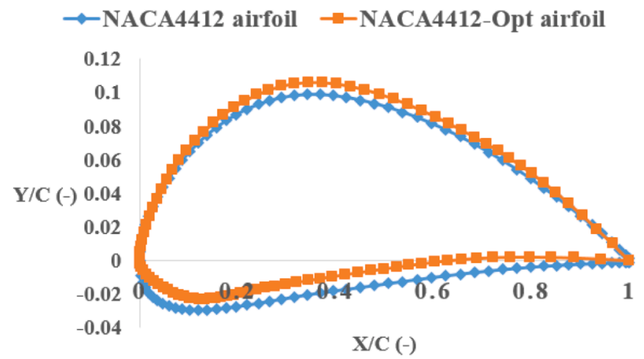

(b) NACA4412

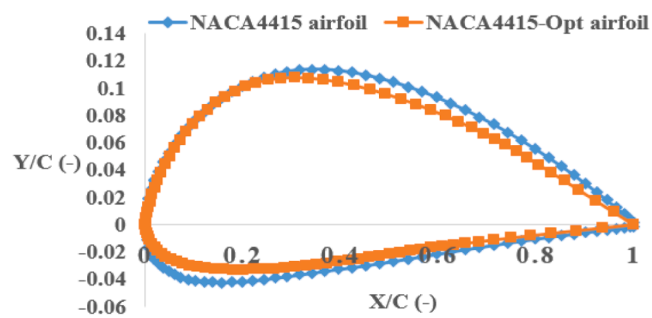

(c) NACA4415

Fig. 5. Airfoils geometry variation for the airfoils optimization.

adjusted according to the velocity update. This iterative process allows the swarm to efficiently explore the parameter space (design space of airfoil geometries), seeking the optimal configuration that maximizes the C_p.

4. Convergence: The swarm continues to iterate through the search space until the PSO algorithm converges to an optimal solution. This optimal solution corresponds to the airfoil geometry with the best aerodynamic performance at the given Re_c of 45,192

The objective function for this optimization was the maximization of the C_p, which serves as the primary indicator of aerodynamic performance.

We calculated the C_p for each airfoil configuration across the λ range, and the optimization process aimed to identify the airfoil geometry that maximized this C_p. Optimizing the TCR improved the flow characteristics and increased the C_p of the NACA0015, NACA4412, and NACA4415 airfoils compared to the original designs. This led to better aerodynamic efficiency, especially at a Re_c of 45,192, where the optimization was performed.

The optimization results indicate a significant increase in the C_p across different λ values, emphasizing the effectiveness of the PSO algorithm in enhancing aerodynamic efficiency. By preserving the symmetrical characteristics of the NACA0015 airfoil and leaving the camber unchanged, the design remained within the category of symmetrical airfoils. The PSO algorithm successfully identified the optimal balance of thickness and TCR to maximize power output. This study demonstrates the capability of the PSO algorithm to optimize airfoil geometries for specific operational conditions, such as those relevant to WT blades or other high-efficiency aerodynamic applications.

3.2. Investigating the C_p of three rotors

Fig. 6 illustrates the variation in the C_p for several rotor airfoils, including NACA0015, NACA0015-Opt, NACA4412, NACA4412-Opt, NACA4415, and NACA4415-Opt, at a Re_c of 45,192. The analysis was performed across a λ range of 0 to 3, using a step size of 0.5, revealing distinct performance disparities between the optimized and non-optimized airfoils. Specifically, the optimized rotors—NACA0015-Opt, NACA4412-Opt, and NACA4415-Opt—consistently demonstrated superior C_p values compared to their non-optimized counterparts.

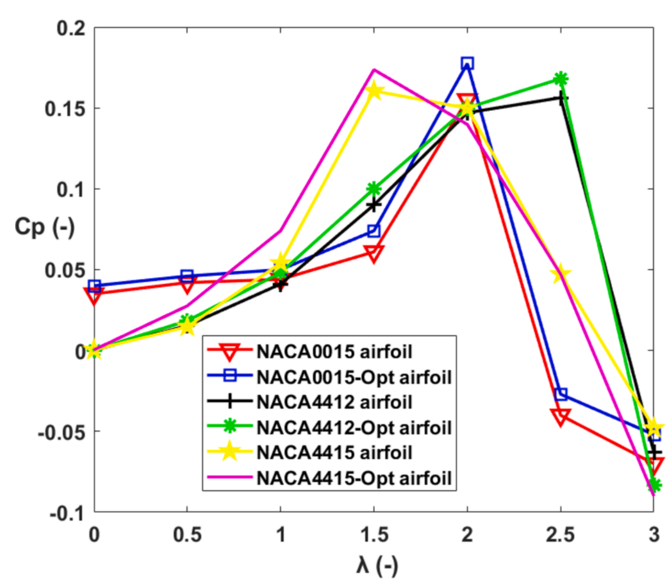

Fig. 6. The C_p variation with the λ of DVAWT rotor efficiencies for rotors.

Notably, the NACA0015-Opt rotor exhibited the highest peak C_p value of 0.1774, a significant 14.45 % improvement over the NACA0015 rotor, which attained a maximum $C_p = 0.1550$. Similarly, optimizing the NACA4412 rotor resulted in a 7.63 % increment in its peak C_p, improving from 0.1563 to 0.1682. The NACA4415 rotor also experienced an 8.15 % improvement in its maximum C_p, rising from 0.1605 to 0.1736 following optimization.

Given the substantial performance gains observed, particularly with the NACA0015-Opt rotor, we selected it for further fabrication and experimental studies. Existing research also supports this selection, demonstrating that, among symmetrical airfoil profiles, the NACA0015 offers the most favorable characteristics, including a reduced rotor dead zone at low λ and superior C_p distribution across the entire λ range [140,141].

The findings of this research highlight the substantial impact of optimization on rotor performance. The NACA0015-Opt rotor achieved a peak C_p of 0.1774, marking a 14.45 % improvement over the traditional NACA0015 rotor, which had a maximum C_p of 0.1550. Similarly, optimization enhanced the NACA4412 rotor's maximum C_p by 7.63 %, from 0.1563 to 0.1682, and the NACA4415 rotor's C_p by 8.15 %, increasing it from 0.1605 to 0.1736.

This research highlights the significant impact of optimization on rotor performance. The NACA0015-Opt rotor achieved a peak $C_p = 0.1774$, reflecting a 14.45 % improvement over the traditional NACA0015 rotor, which had a maximum $C_p = 0.1550$.

Similarly, optimization increased the maximum C_p of the NACA4412 rotor by 7.63 %, from 0.1563 to 0.1682, while the NACA4415 rotor saw an 8.15 % improvement, with its C_p rising from 0.1605 to 0.1736.

In comparison to other studies, the improvements achieved here are particularly notable. Zhang et al. [142] observed increases in C_p ranging from 3.42 % to 7.35 % for a bionic airfoil, significantly lower than the 14.45 % enhancement seen with the NACA0015-Opt rotor. Similarly, Abul-Ela et al. [143] indicated a peak $C_p = 0.3263$ for the NACA0021 rotor at a $\lambda = 2.63$, without utilizing the optimization techniques applied in the present work.

Other advancements, such as the airfoil developed with negative camber that improved average torque by 8.8 % [144] or the circular dimples that increased C_p by 5.18 % [145], also lack the enhancements seen in the NACA0015-Opt. Kord and Bazarghan [146] found that optimizing the inboard configuration of J-shaped DVAWTs increased power generation by 12.35 % at higher λ. However, the NACA0015-Opt rotor consistently outperforms it across various λ, highlighting its superior aerodynamic efficiency. Likewise, the 7 % boost in C_p from leading-edge serrations [147] and the 10.5 % gain from blade length extensions [148] demonstrate the effectiveness of optimization in achieving comparable or superior outcomes.

Studies show that auxiliary DVAWTs can achieve 5 % higher C_p than traditional rotors [149], and blades with homogeneous surface irregularity improve C_L/C_D by approximately 12 % across all β [104]. Variable swept area (A) blades enhance C_T, reaching a$C_T = 0.30$ [150], while porous deflectors increase C_p by 10 % at λ of 1 [151]. Semi-flexible trailing edges broaden the operational range, improving performance by 10 % [152], and gust inclusion boosts the C_p of helical VAWTs by 1.97 % [153]. Despite these advances, the NACA0015-Opt rotor shows superior and consistent gains across various λ.

While vented airfoils resulted in a 20 % increase in torque at low λ [154], this was accompanied by reductions in C_p at higher λ, emphasizing the advantage of optimized airfoils like the NACA0015-Opt in maintaining superior performance across different λ ranges. Similarly, design modifications such as long-wavelength bumps [155] and flexible rotors [156] achieved increases in C_p of 6.28 % and up to 9.6 %, respectively—improvements still less pronounced than those achieved in this study.

Guo et al. [157] studied a hybrid turbine that integrates a Φ-shaped rotor with a DVAWT, achieving a peak C_p of 0.02531. Additionally, blades with slit Gurney flaps indicated an 8 % decrement in C_D at $\lambda = 2.64$ but a 2 % decrement in C_L in comparison with standard Gurney flaps. This incremented lift-to-drag ratio (C_L/C_D), increasing power output by 6.5 % at $\lambda = 2.64$ [158].

Overall, the findings of this study emphasize the effectiveness of optimization in improving the aerodynamic efficiency of VAWTs. The NACA0015-Opt rotor achieves improvements that surpass many previously reported methods, including the use of auxiliary rotors, porous deflectors, blades with semi-flexible trailing edges, or advanced designs like Φ-shaped hybrid rotors and slit Gurney flap blades. In contrast to approaches requiring complex configurations or external devices, the NACA0015-Opt rotor achieves efficiency solely through airfoil optimization, offering a simpler and more cost-effective solution. This ensures superior and reliable performance across various circumstances, establishing it as a robust and efficient design for maximizing C_p in VAWTs.

4. Design and fabrication of the DVAWT prototype

Many researchers have examined the impact of SBs on the self-starting efficiency of DVAWTs, including research by Peng et al. [111], Guo et al. [159,160], Maeda et al. [135], Li et al. [161], Wang et al. [162], and Xu et al. [163]. In this study, DVAWT blades were fabricated with two types of surface finishes: smooth and embossed, the latter created using embossed sheet material.

The objective was to compare the *AR* impact on the startup efficiency of a DVAWT equipped with SBs versus one with EBs. Aerodynamic and practical considerations drove the selection of an embossed aluminum sheet to introduce roughness to the DVAWT blades. This material features a textured surface resembling crocodile skin, which enhances friction and prevents slippage, offering several advantages in terms of aerodynamic performance and operational efficiency.

From an aerodynamic standpoint, the roughness introduced by the embossed pattern promotes the development of a turbulent boundary layer on the airfoil surface. This turbulence helps delay flow separation, a critical factor for maintaining lift. By keeping the airflow attached to the blade for a longer duration, the C_L/C_D is optimized, thereby improving the aerodynamic effectiveness of the DVAWT, notably at low λ and during startup. Consequently, the rougher surface texture facilitates the generation of higher lift forces (F_L), essential for efficient power generation and the self-starting behavior of the DVAWT.

The embossed surface not only enhances lift but also boosts torque production, especially during startup, by improving the wind's interaction with the rotor blades. The increased friction minimizes slippage, ensuring a more consistent and efficient transfer of force from the wind to the rotor. This is especially critical for self-starting capabilities, as the torque generated at LWVs is essential for overcoming initial inertia and initiating rotation without external assistance.

Moreover, the embossed sheet material helps minimize excessive drag, a common concern with rough surfaces. By utilizing an embossed pattern, the increase in drag is controlled and balanced, ensuring that the benefits in lift generation outweigh any potential drag losses. This careful management of drag is crucial for maintaining efficient operation across varying λ, preventing excessive torque losses that could hinder DVAWT performance at higher rotational speeds.

An additional essential benefit is the enhancement of self-starting capability. The textured surface reduces the likelihood of flow separation. It facilitates a better interaction between the blades and the wind, improving the DVAWT's ability to self-start, even in LWV conditions. The embossed pattern helps "grip" the wind, increasing the likelihood of the rotor blades initiating movement and reducing the risk of stalling under challenging conditions.

The use of embossed aluminum directly enhances the aerodynamic stability of the DVAWT. The induced turbulence contributes to more stable airflow around the blades, ensuring smoother and more predictable performance. This stability is especially important for maintaining consistent operation in variable wind conditions, ensuring that the

DVAWT performs efficiently across various operational scenarios.

A computer-controlled laser cutter was used in the material-cutting process to achieve precise and accurate blade shapes. This advanced machining technique enabled high precision and consistency in fabricating the DVAWT components. As depicted in Fig. 7, two variations of aluminum blade materials, both with a thickness of 0.0003 m, were utilized. These materials included both smooth and embossed surfaces, chosen to cover specific sections of the blades. The embossed material, in particular, was selected for its potential to enhance aerodynamic performance, as it facilitates improved friction and flow interaction with the wind, thus optimizing the DVAWT's efficiency.

For the structural integrity of the VAWT, a circular-section aluminum pole was opted. This pole served as the central structural element, providing robust support to the system. To further reinforce the stability of the VAWT, additional structural components were attached to the pole at intervals of 8.75 cm, ensuring that the assembly remained rigid and capable of withstanding operational stresses.

We made the central shaft of the DVAWT from a 0.020 m diameter iron tube, selecting it for its durability and strength. Iron, being a sturdy material, was ideal for supporting the rotational forces generated by the WT during operation.

Six iron tubes, each with a radius (R) of 0.020 m, were used to connect the VAWT blades to the central shaft. These tubes provided a secure and stable connection between the blades and the shaft, ensuring proper alignment and minimizing any potential mechanical failure during the VAWT's operation.

This approach, which combines advanced manufacturing techniques with carefully selected materials, ensures both the aerodynamic performance and framework stability of the DVAWT. Using a computer-controlled laser cutter not only guarantees precision but also allows for the efficient production of components that meet the rigorous design requirements for optimal VAWT performance. Furthermore, the choice of materials, including aluminum for the blades and iron for the shaft and connecting tubes, was driven by their strength-to-weight ratio, corrosion resistance, and suitability for the operational environment, thus enhancing the overall sustainability and longevity of the VAWT.

Fig. 8 provides a three-dimensional representation of the Dual VAWT, offering a detailed visualization of its structural configuration. In conjunction with this, Table 2 outlines the key parameters associated with the VAWT, presenting their respective values for reference.

Among these parameters, the AR is especially important, as it significantly influences the aerodynamic performance and overall effectiveness of the DVAWT. The AR is the ratio of the rotor's H to its D, as illustrated in Equation 2. This geometric parameter is essential for understanding the VAWT's performance, as it influences both the efficiency of the energy capture and the mechanical stresses the system may experience during operation. A higher AR typically results in a more efficient VAWT design, as it allows for better utilization of the wind flow. In comparison, a lower AR may lead to reduced aerodynamic efficiency and higher turbulence around the blades.

The AR is a critical design factor because it affects several operational aspects of the WT. A VAWT with an appropriate AR can optimize the distribution of forces across the rotor blades, improving power generation while minimizing drag and other inefficiencies. The AR also influences the VAWT's stability and the dynamic behavior of the rotor in varying wind conditions. Thus, careful consideration and optimization of this parameter are essential for achieving the desired performance characteristics of the DVAWT.

$$AR = \frac{H}{D} \tag{3}$$

We selected an initial AR of 1 for the DVAWT, a value that previous studies [164] have shown corresponds to the highest λ and optimal aerodynamic efficiency for small-scale DVAWTs. This AR value represents a balanced design, where the H of the rotor is proportional to its D, facilitating an efficient interaction between the rotor blades and the wind flow. The choice of AR is critical as it directly influences the VAWT's performance by affecting the F_L and drag force (F_D) acting on the blades, the flow dynamics around the rotor, and ultimately, the VAWT's ability to generate power at various U_∞. Thus, setting the AR to 1 aligns with established findings that maximize the VAWT's operational efficiency, particularly for small-scale applications where compactness and efficiency are crucial design objectives.

S is a key design parameter used to characterize the geometry of a wind turbine, specifically its rotor. It defines the ratio of the area covered by the turbine blades to the total area of the rotor. In simpler terms, S shows the proportion of the rotor occupied by blades [140]. The formula for calculating S is:

$$S = \frac{NC}{D} \tag{4}$$

The S of the VAWT, where N represents the number of blades, is calculated to be 0.608 for a three-bladed VAWT design with a R of 0.175 m and a C of 0.071 m.

To improve the self-starting abilities of the DVAWT, increasing the blade C was implemented as a strategic design modification. This adjustment was explicitly aimed at improving the VAWT's low starting torque, a critical parameter for VAWTs. A higher starting torque ensures a more favorable force-to-friction ratio, enabling quicker and more reliable self-starting under varying U_∞ conditions. This is particularly important for DVAWTs, as efficient startup performance directly impacts their overall operational efficiency and ability to harness wind energy effectively.

(a) Smooth sheet

(b) Embossed sheet

Fig. 7. Blade material used: a) smooth sheet and b) embossed sheet.

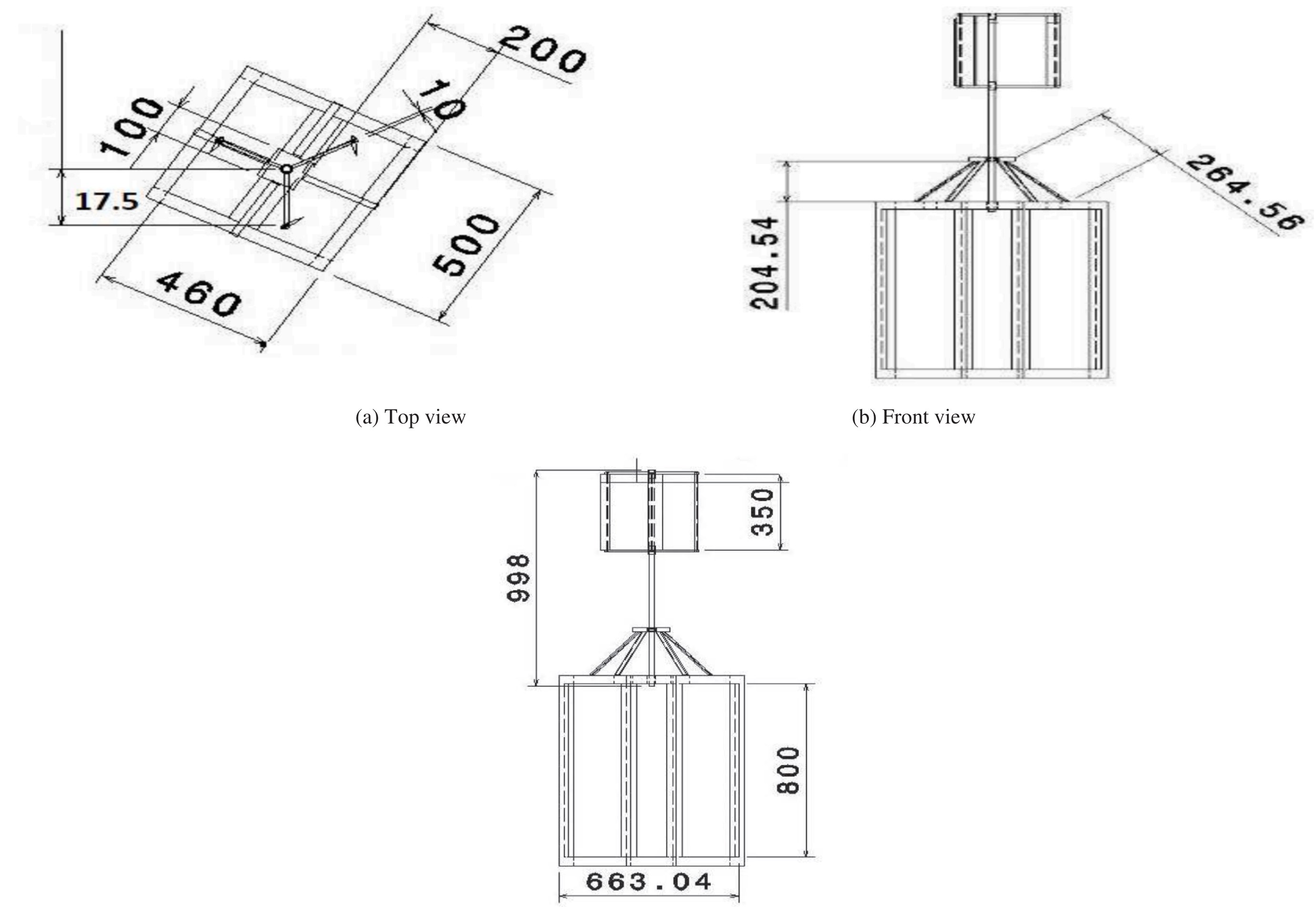

(a) Top view (b) Front view

(c) Side view

Fig. 8. Rotor shape (drawing computer-aided design (CAD)) with three views: (a) Top view, (b) Front view, and (c) Side view.

Table 2
Geometric characteristics of the DVAWT.

Parameters	Value
R	0.175 m
H	0.35 m
C	0.071 m
S	0.608
AR	1
N	3
Shaft diameter	0.02 m
Number of arms	6
Twist angle	0°

We assembled the VAWT with meticulous attention to structural integrity and durability. The arms connecting the blades to the central shaft used the shielded metal arc welding (SMAW) technique.

We chose this welding method for its ability to provide a high-quality surface finish, strong adhesion between components, and cost-efficiency, making it particularly suitable for small-scale WT construction [165]. SMAW ensured the robustness of the connections while minimizing fabrication costs, a critical consideration in sustainable VAWT design.

Fig. 9 provides a detailed view of the assembled DVAWT, showcasing the integration of the enhanced C blades and welded components. This assembly method enhances both the aerodynamic and mechanical stability of the VAWT, while also reflecting a design strategy that balances cost-effective construction with optimized performance. These innovations helped refine the VAWT design, improving startup behavior, durability, and energy capture efficiency.

In this study, fan blowers were used to simulate wind conditions similar to those found in real-life environments. The experimental wind source consisted of a 2x2 arrangement of four fan blowers (Fig. 10b). The distance between the blower fans and the DVAWT shaft was set at 1 m to achieve stable and uniform airflow, by conditions used in previous studies to ensure uniform U_∞ [166–169].

Before each experiment, we turned on the fans and allowed a waiting time of five minutes for the airflow to stabilize and become uniform. This waiting time ensures that the wind has reached a steady state and that no significant fluctuations in U_∞ are present.

To control the U_∞, a dimmer was installed between the blowers and the power source, enabling the fan speed to be adjusted within a range of 0.5 to 11 m/s.

In other words, a dimmer device controlled the U_∞, regulating the airflow between 0.5 m/s and 11 m/s. The U_∞ output from the blowers was measured using an anemometer capable of measuring speeds with an accuracy of $\pm$ 0.5 m/s.

Furthermore, to ensure precise measurement of the U_∞, the U_∞ was measured at 9 different points using a handheld anemometer. Data were recorded five times at 30-second intervals to ensure measurement accuracy.

In this study, we examined eight DVAWT models. We placed all the DVAWTs 1 m apart and used identical experimental conditions for each model. To examine the performance of the three-blade DVAWTs, a force meter with an accuracy of $\pm$ 2 % was employed to measure the startup

(a) Assembled CAD Model (b) Assembled SB-DVAWT

(c) Assembled EB-DVAWT

Fig. 9. Constructed (a) CAD Model, (b) SB-DVAWT, and (c) EB-DVAWT.

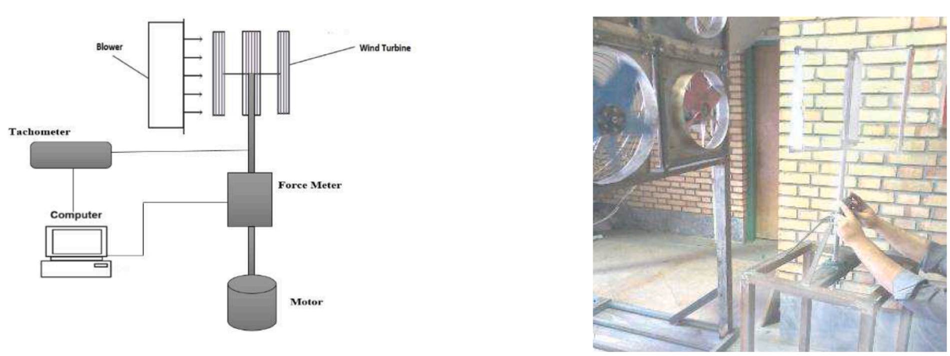

(a) Schematic VAWT (b) Test VAWT

Fig. 10. Test configuration: (a) diagram and (b) the experimental VAWT.

torque. This device measures the forces applied to the turbine and is directly attached to the central shaft of the to measure the force acting on the shaft accurately. Subsequently, the measured force, combined with the distance from the center of the shaft, was used to calculate the torque.

The torque is determined by multiplying the measured force by the distance from the axis of rotation.

To precisely measure the startup torque required for the DVAWTs, data from the force meter were collected. We measured the force for each experiment and repeated the process ten times for each variation in experimental conditions to ensure the dependability and repeatability of the results. We recorded all results under identical conditions for each of the eight DVAWT models, allowing for a precise comparison of the torque produced by each.

Fig. 10a provides a schematic diagram of the experimental setup. To examine the effect of the *H* of the embossed-bladed DVAWT on its self-starting capabilities, eight different scenarios were studied, as outlined in Table 3.

We meticulously fixed the central shaft of the DVAWT at two crucial points using a precision-engineered bearing mechanism. We specifically

Table 3
The eight scenarios examined in this study.

Scenario	
1	NACA0015 rotor for SB-DVAWT with a H of 35 cm ($AR = 1$)
2	NACA0015 rotor for an EB-DVAWT with a H of 35 cm ($AR = 1$)
3	NACA0015-Opt rotor for a SB-DVAWT with a H of 35 cm ($AR = 1$)
4	NACA0015-Opt rotor for an EB-DVAWT with a H of 35 cm ($AR = 1$)
5	NACA0015 rotor for a SB-DVAWT with a H of 75 cm ($AR = 2.14$)
6	NACA0015 rotor for an EB-DVAWT with a H of 75 cm ($AR = 2.14$)
7	NACA0015-Opt rotor for a SB-DVAWT with a H of 75 cm ($AR = 2.14$)
8	NACA0015-Opt rotor for an EB-DVAWT with a H of 75 cm ($AR = 2.14$)

designed this system to minimize mechanical vibrations and ensure smooth rotational motion, which are essential for the VAWT's operational efficiency and structural longevity. The reduction of vibrations not only enhances the VAWT's performance and minimizes wear and tear on components, contributing to a more reliable and durable energy generation system.

To improve the VAWT's stability during operation, especially under changing wind conditions, we implemented a strong counterweight mechanism. Four iron plates, each weighing 25 kg, were strategically positioned to provide the necessary balance and support.

The plates were strategically placed to correct any imbalances in the rotor assembly and ensure the VAWT maintained a stable rotation axis. Adding these weights was crucial in mitigating oscillations and reducing stress on the bearings and shaft, which could otherwise compromise the VAWT's performance and structural integrity.

This combination of a vibration-dampening bearing system and strategically placed counterweights underscores a comprehensive approach to mechanical stabilization. By addressing dynamic and static stability concerns, the design ensures optimal performance, reduced maintenance requirements, and an extended operational lifespan for the DVAWT. These measures highlight the integration of precision engineering and practical solutions to establish a trustworthy and effective wind power configuration.

5. Results and discussion

5.1. Experimental errors types

The specific sources of error encountered in this study are listed below, reflecting potential limitations inherent to the experimental procedures and equipment precision:

1. U_∞ Measurement errors

During wind tunnel testing, an anemometer and a sensor measured the blower speed. Despite employing these dual instruments for cross-verification, measurement inaccuracies likely occurred. These discrepancies may have arisen from calibration imperfections, instrument sensitivity limitations, or environmental factors such as turbulence and flow instability within the testing area.

2. Manual positioning of the DVAWT model

We used an indicator clock, a template, and a digital level to manually align and position the DVAWT model for different test configurations. While this approach allowed flexibility in the setup, it also introduced potential human error. Factors such as inconsistencies in visual alignment, minor deviations in tool application, and physical fatigue during repetitive adjustments could have contributed to imprecision in distance or angular positioning, ultimately affecting the reproducibility of the results.

3. Manufacturing inaccuracies

The fabrication process of the DVAWT model, which involved intricate assembly and material handling, may have introduced minor structural inaccuracies. These imperfections could have led to deviations from the intended aerodynamic profile, thereby influencing the flow behavior around the blades and affecting the performance metrics captured during testing.

4. Measurement device limitations

Despite rigorous calibration protocols for instruments such as force meters, tachometers, and anemometers, we cannot entirely rule out errors in data recording. Each device is subject to inherent accuracy limitations, with an error margin of ± 0.2 % in this study. While minimal, such precision constraints could compound when we integrated multiple measurements to derive performance parameters, potentially resulting in discrepancies in the final data analysis.

These identified sources of error highlight the challenges inherent in experimental studies involving complex systems like DVAWTs. Although we made every effort to reduce these limitations through careful calibration, standardized procedures, and repeated trials, some residual inaccuracies were inevitable.

Acknowledging these errors is critical for contextualizing the study's findings and guiding future work to enhance experimental precision. Such improvements could include employing automated positioning systems, adopting higher-precision manufacturing techniques, and using advanced measurement instruments with reduced error margins.

5.2. Detailed calculations of resisting torques (T_{Resist}) and their relation to aerodynamic torque (T_A)

The self-starting capability of DVAWTs is significantly affected by resistive torques, including friction, inertia, and aerodynamic drag. These opposing forces hinder the rotational motion of the VAWT, particularly at LWVs, where external assistance is often necessary to overcome the initial resistance. A comprehensive analysis of these resistive torques and their interplay with the T_A is essential for understanding and optimizing the self-starting performance of DVAWTs. The subsequent sections detail the primary resistive torques acting on the VAWT and their respective mathematical formulations.

5.2.1. Frictional torque (T_f)

T_f is generated by the interaction between the blade surface and the surrounding air, along with internal friction within the rotating components of the VAWT. At LWVs, this torque becomes a critical factor in opposing the VAWT's motion. The T_f can be determined using the following equation:

$$T_f = \mu F_N R \quad (4)$$

where μ is the coefficient of friction, which depends on the material and surface roughness of the blades, F_N is the normal force acting on the blade, determined either experimentally or through simulations. This T_f increases with the blade surface roughness and resistance to air movement, which contribute to the torque required for self-starting.

5.2.2. Inertia torque (T_I)

Inertial torque arises from the VAWT's resistance to changes in its rotational velocity, which resists acceleration or deceleration during operation. This torque is particularly significant during the startup phase, as the VAWT must overcome its inertia to initiate rotation. The following equation defines the inertial torque:

$$T_I = I\alpha \quad (5)$$

Where I represent the rotor's moment of inertia, which for a circular rotor is calculated as:

$$I = \frac{1}{2}mR^2 \quad (6)$$

with m is the mass of the rotor and α is the angular acceleration, which denotes the rate of change in rotational velocity. Reducing the moment of inertia or enhancing the efficiency of the initial startup phase can mitigate the resistance caused by inertia, thereby improving the VAWT's self-starting performance.

5.2.3. Aerodynamic drag torque (T_D)

T_D results from the resistance exerted by the air against the rotating blades. This force becomes particularly significant at high U_∞ and when the blades rotate at considerable velocities. The T_D can be calculated using the following equation:

$$T_D = \frac{1}{2}C_D\rho AU_\infty^2 R \quad (7)$$

Where A is computed as $A = H.\ C$. This T_D opposes the motion of the blades and adds to the total T_{Resist} that the VAWT must overcome to initiate rotation.

5.2.4. TheT_A

T_A is the torque produced by the aerodynamic forces acting on the blades, which serves as the primary driving force for rotation in a VAWT. This torque is responsible for overcoming the resistive forces and can be calculated as follows:

$$T_A = \frac{1}{2}C_L\rho AU_\infty^2 R \quad (8)$$

This T_A is responsible for initiating the VAWT's rotation and overcoming the resistive torques.

5.2.5. Mathematical relationship between resistive torques andT_A

To quantify the effect of the T_{Resist}(T_f, T_I, and T_D) on the $T_{Self-starting}$, it is crucial to examine how these forces relate to the total T_A. At LWVs, the T_{Resist} dominates, and minimizing it is essential to enable effective self-starting. The following equation represents the total T_{Resist}:

$$T_{resist} = T_f + T_I + T_D \quad (9)$$

The $T_{Self-starting}$ is the torque required to overcome the total T_{Resist} and initiate the rotation of the VAWT. The T_A must exceed the T_{Resist} for the VAWT to begin rotating.

5.2.6. Impact of U_∞ on$T_{Self-starting}$

Experimental results show that as U_∞ increases, both aerodynamic and T_{Resist} increase. However, T_A typically increases at a faster rate, resulting in a reduction in the required $T_{Self-starting}$. The relationship between U_∞ and $T_{Self-starting}$ is expressed as follows:

$$T_{Self-starting}(U_\infty) = T_{resist}(U_\infty) - T_A(U_\infty) \quad (10)$$

We can use this equation to compare the $T_{Self-starting}$ at different U_∞. By analyzing this relationship, we can gain a deeper understanding of how varying U_∞ affects the self-starting capability and optimize the VAWT's design accordingly. Therefore, we can mathematically express the variation in $T_{Self-starting}$ with increasing U_∞ as follows:

The calculation of the resistive torques (T_f, T_I, and T_D) and their relationship with the T_A provides a comprehensive understanding of the forces that influence the self-starting capability of DVAWTs. By addressing these resistive forces through design modifications—such as optimizing the airfoil shape, employing EBs, and adjusting H—it is possible to reduce the required $T_{Self-starting}$ and enhance the VAWT's overall performance. These calculations and their implications are crucial for further advancing the design of DVAWTs, particularly in LWV conditions, where self-starting poses a significant challenge.

5.3. Testing study of the $T_{Self-starting}$ demanded by the DVAWT

The initial torque needed to surpass inertia and initiate the rotation of a DVAWT is essential for its operation, particularly at lower U_∞. This torque is required in order to overcome the VAWT's resistance to motion, which includes both aerodynamic and mechanical resistances. At LWVs, the initial torque required to start the VAWT is significantly higher than the energy the VAWT can generate once it reaches its operational speeds. Therefore, reducing this initial torque is crucial for improving the overall efficiency of WTs, as it directly affects the energy consumed during startup and, consequently, the energy available for power generation.

5.3.1. Comparisons of the torque required to start a DVAWT at a H of 35 cm

Fig. 11 compares the required $T_{Self-starting}$ for the NACA0015 and NACA0015-Opt rotors, using both SB-DVAWT and EB-DVAWT at various U_∞, specifically at a H of 35 cm. Due to the inherently poor self-starting characteristics of DVAWTs at LWVs, these DVAWTs require significantly higher starting torque to initiate rotation at lower U_∞ compared to moderate or higher U_∞. At LWVs, the aerodynamic forces acting on the blades are insufficient to overcome resistance and initiate rotation, necessitating a higher $T_{Self-starting}$.

Notably, in the absence of wind, neither DVAWT can overcome the initial resistance, resulting in zero startup torque. This emphasizes the importance of U_∞ in providing the necessary aerodynamic forces to overcome resistive torques, such as inertia and friction, and initiate DVAWT rotation. In Fig. 11, it is evident that at a U_∞ of 1 m/s, EB-DVAWTs show a considerable decrease in the necessary $T_{Self-starting}$ compared to those with SBs. Specifically, the NACA0015-Opt rotor with EB-DVAWT achieves a $T_{Self-starting}$ of 0.1425 Nm, a notable improvement over its SB counterpart.

At this LWV, the T_A generated by the airfoil design, especially in the case of EB-DVAWTs, plays a crucial role. Typically, at lower U_∞, T_A is insufficient to easily overcome the T_{Resist}, which includes T_I, T_f, and T_D. The EBs design addresses this issue by reducing T_D through an enhanced airflow pattern that smooths the flow over the blade surface, decreasing resistance and thus lowering the $T_{Self-starting}$ requirement.

Combining the NACA0015-Opt rotor with EBs optimizes the C_L/C_D of the DVAWT. This modification increases lift while reducing drag at LWVs, critical for self-starting in DVAWTs. By reducing drag, the total resisting torques (T_f, T_I, and T_D) are decreased, allowing the T_A to overcome these resistances more easily. This explains why, at 1 m/s, the EB-DVAWT with NACA0015-Opt rotor requires less torque to initiate rotation than the standard NACA0015 with SBs.

In the case of a U_∞ of 2 m/s, the reduction in $T_{Self-starting}$ observed across each DVAWT aligns with the increase in available T_A as U_∞ rises. At this U_∞, both the EBs and the optimized NACA0015 rotor showed a clear advantage in reducing the torque required to overcome resisting forces and initiate rotation. For EB-DVAWTs, the required $T_{Self-starting}$ decreased from 0.14 Nm to 0.126 Nm. This reduction results from the improved aerodynamic profile provided by the EB surface, which smooths the airflow and enhances lift characteristics, thereby reducing aerodynamic T_D. Consequently, this leads to a lower total $T_{Self-starting}$, as T_A becomes sufficient to counteract T_{Resist} more effectively at 2 m/s.

Similarly, for SB-DVAWTs using the optimized NACA0015 rotor, the required $T_{Self-starting}$ decreased from 0.14 Nm to 0.13475 Nm. This reduction reflects how adjustments to the airfoil's C and TCR improve the C_L/C_D, enhancing the effectiveness of T_A in initiating DVAWT rotation. These changes in airfoil geometry also decrease T_D, the drag component, enabling the SB-DVAWT to start rotating at a lower threshold of $T_{Self-starting}$.

Overall, the experimental results at 2 m/s validate that modifications to the blade embossing and airfoil design substantially benefit the DVAWT's self-starting capability. By optimizing T_D through reduced

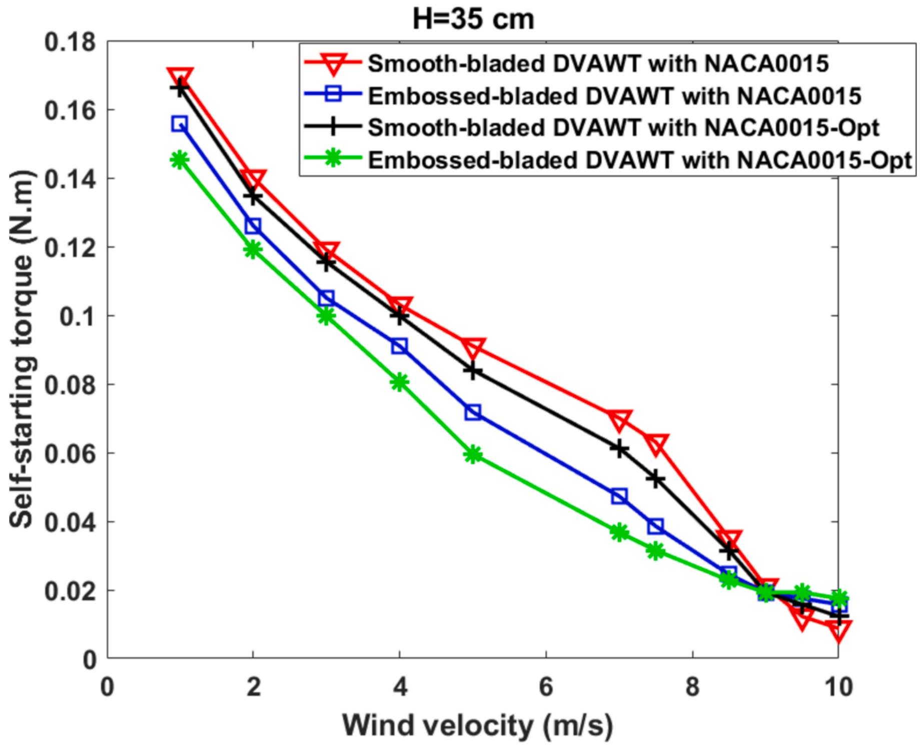

Fig. 11. Comparison of $T_{Self-starting}$ required at different U_∞ at a H of 35 cm.

drag and improving lift, the T_A can more easily overcome T_I and T_f, allowing the DVAWT to self-start with less input from the wind.

At a U_∞ of 3 m/s, the $T_{Self-starting}$ required for each DVAWT continued to decrease compared to the lower U_∞ of 2 m/s. The trend observed at 3 m/s mirrors the results at the lower U_∞, with the EB-DVAWT with optimized NACA0015 rotor requiring the least $T_{Self-starting}$. This further emphasizes the positive impact of these modifications on DVAWT performance, particularly in reducing the energy needed to overcome initial resistance and initiate rotation.

The improved aerodynamic performance of the EBs and the optimized NACA0015 rotor leads to a decrease in $T_{Self-starting}$. As U_∞ increases, the T_A becomes more significant, allowing it to effectively counteract the T_{Resist}, including T_f, T_I, and T_D. The EBs, which reduce drag and enhance lift, enable the DVAWT to overcome these resisting forces with less effort.

At 3 m/s, the SB-DVAWT with the traditional NACA0015 rotor needed the Greatest $T_{Self-starting}$ among all configurations. This matches the findings at lower U_∞, where the standard SB profile, combined with the original airfoil geometry, creates more drag and less efficient lift. As a result, the SB-DVAWT has more difficulty overcoming T_{Resist} at this U_∞, leading to a higher $T_{Self-starting}$ requirement.

In summary, the results at 3 m/s further validate the effectiveness of using EBs and optimized airfoils in reducing the $T_{Self-starting}$. These modifications facilitate the conversion of wind energy into rotational energy with greater efficiency, requiring less initial force to initiate the DVAWT's rotation, particularly as U_∞ increases. The combined Darrieus-Savonius turbine in the same study showed better performance, self-starting at 2.81 m/s and outperforming the traditional DVAWT design. In contrast, an effort on traditional symmetric rotor DVAWTs revealed that it struggled to produce significant power output until the U_∞ reached 3.65 m/s [170]. However, our results show that EB-DVAWTs exceed the self-starting capabilities of both traditional DVAWT and hybrid Darrieus-Savonius VAWT.

At a U_∞ of 4 m/s, the $T_{Self-starting}$ for each DVAWT continued to follow the pattern seen at lower U_∞, showing a notable reduction in torque requirements for configurations with EBs and optimized airfoils The SB-DVAWT rotor with the original NACA0015 rotor served as the baseline, requiring a $T_{Self-starting}$ of 0.103 Nm. This value served as the reference point for comparing all other configurations.

The EB rotor with the NACA0015 rotor demonstrated an 11.65 % improvement, requiring only 0.091 Nm of $T_{Self-starting}$. This reduction results from the aerodynamic advantages of the EBs, which decrease drag, enhance lift, and lower overall resistance to initial motion. These improvements make it easier for the DVAWT to overcome the T_{Resist}—T_f, T_I, and T_D—and initiate rotation.

In comparison, the SB-DVAWT rotor with the NACA0015-Opt rotor required a $T_{Self-starting}$ of 0.09975 Nm, representing a 3.14 % improvement over the SB-DVAWT rotor with the original NACA0015 rotor. While this reduction reflects the positive impact of optimizing the airfoil design, the improvement is less pronounced than that achieved with the EBs. The NACA0015-Opt rotor modifications enhance the C_L/C_D, reducing drag and improving overall aerodynamic performance; however, the effect is more modest compared to the substantial benefits provided by EBs.

Finally, the configuration with the EBs rotor and the NACA0015-Opt rotor exhibited the lowest $T_{Self-starting}$ of 0.0805 Nm, marking a 21.97 % improvement over the SB-DVAWT with the NACA0015 rotor. This configuration delivered the best performance in $T_{Self-starting}$, requiring the least torque to initiate rotation. A rotor with triangular dimples showed a 13.6 % performance improvement over the traditional DVAWT at 4 m/s [171].

At $U_\infty = 5$ m/s, the $T_{Self-starting}$ for each DVAWT decreased compared to lower U_∞. The trend observed at 5 m/s is consistent with the results at lower U_∞, with the DVAWT equipped with EBs and the optimized NACA0015-Opt rotor requiring the least $T_{Self-starting}$. This further highlights the positive influence of these alterations on DVAWT performance, particularly in reducing the energy needed to overcome initial resistance and initiate rotation.

The decrease in $T_{Self-starting}$ can be due to the superior aerodynamic performance of the EBs and the optimized NACA0015 rotor. As U_∞ increases, the T_A becomes more dominant, enabling it to counteract the T_{Resist}—including T_f, T_I, and T_D—more effectively. The EBs, which reduce drag and enhance lift, allow the DVAWT to overcome these resisting forces with less effort.

At $U_\infty = 5$ m/s, the SB-DVAWT utilizing the NACA0015 rotor exhibited the highest $T_{Self-starting}$ among all configurations, consistent with findings at lower U_∞. The SB profile, combined with the original airfoil geometry, generates higher drag and less efficient lift, making it more difficult for the DVAWT to overcome the T_{Resist} at this U_∞.

In comparison, the SB-DVAWT utilizing the NACA0015-Opt rotor required a $T_{Self-starting} = 0.084$ Nm, reflecting an 18.45 % improvement over the baseline SB-DVAWT with the NACA0015 rotor. This improvement results from the optimized NACA0015 rotor design, which reduces drag and enhances lift, enabling the DVAWT to overcome resisting forces more efficiently.

The EB-DVAWT utilizing the NACA0015 rotor required a $T_{Self-starting} = 0.091$ Nm, representing an 11.65 % improvement compared to the SB-DVAWT with the NACA0015 rotor. The EBs improve the C_L/C_D, reduce drag, and lower friction, thereby reducing the overall T_{Resist} and facilitating the start of rotation.

The most significant improvement was observed in EB-DVAWT utilizing the NACA0015-Opt rotor, which needed a $T_{Self-starting}$ of just 0.0595 Nm—a remarkable 42.72 % reduction compared to the SB-DVAWT with NACA0015 rotor.

Xu et al. [172] evaluated the NACA2418 rotor, which achieved a 20 % reduction in startup time at $\beta = 10^\circ$ at a U_∞ of 5 m/s. Similarly, Kavade et al. [173] found that a VAWT with a NACA0021 airfoil struggled to start at lower U_∞ (1–5 m/s) because of inadequate $T_{Self-starting}$.

At a U_∞ of 7 m/s, significant reductions in $T_{Self-starting}$ are observed across various DVAWT configurations compared to the baseline SB-DVAWT rotor with the NACA0015 rotor, which requires 0.070 Nm of $T_{Self-starting}$. The EB rotor with the NACA0015 rotor demonstrates a 32.14 % reduction, requiring only 0.04725 Nm. This improvement underscores the effectiveness of EBs in reducing resistance and facilitating easier DVAWT startup.

In comparison, the SB-DVAWT rotor with the optimized NACA0015-Opt requires 0.06125 Nm of torque, which is a 12.5 % reduction compared to the baseline. Although the optimized airfoil improves the C_L/C_D and enhances aerodynamic efficiency, its impact on reducing $T_{Self-starting}$ is less pronounced than that of the EBs.

The EB rotor featuring the optimized NACA0015-Opt rotor achieves the most significant improvement, requiring just 0.03675 Nm of $T_{Self-starting}$—a remarkable 47.5 % reduction compared to the baseline. This configuration combines the benefits of EBs and an optimized airfoil, offering the highest efficiency in initiating rotation. It effectively counters T_{Resist} such as T_f, T_I, and aerodynamic T_D. A study on a 3-PB VAWT configuration, which features three blades divided into equal-height segments (H/3), tested with helix angles ranging from 60° to 120° at a U_∞ of 7 m/s, revealed that modifying the helix angle significantly improved performance. Compared to a standard 60° helix angle design, the modified configuration reduced fluctuations in the C_T by 40 % at a lower λ of 0.44, demonstrating enhanced aerodynamic stability [174].

At U_∞ of 7.5 and 8.5 m/s, a consistent reduction in $T_{Self-starting}$ requirements was observed across all four DVAWT configurations, continuing the trend of decreasing startup torque with increasing U_∞. Each DVAWT exhibited lower torque requirements to initiate rotation as U_∞ increased, highlighting the aerodynamic improvements that enhance performance at higher U_∞. The EB design notably reduced drag and resistance, thereby enhancing lift and enabling the DVAWT to overcome T_{Resist} more effectively. This was particularly evident in the reductions observed in T_f, T_I, and T_D, where the EB configuration consistently outperformed the SB design.

Among the design modifications, the EBs had a more significant impact on reducing startup torque than the modification of the NACA0015 rotor shape alone. However, when combined, the altered airfoil and EBs produced a synergistic effect, maximizing aerodynamic efficiency. The optimized NACA0015 rotor enhanced the C_L/C_D, reducing the initial torque required to initiate rotation by increasing T_A while minimizing drag. This dual improvement from the airfoil modification and EB design allowed the DVAWTs to achieve smoother self-starting capabilities, particularly at higher U_∞.

At a U_∞ of 9 m/s, all DVAWT configurations continued to exhibit a decline in startup torque requirements, consistent with the trend observed at lower U_∞. However, the differences in startup torque reductions between configurations became less pronounced at this higher U_∞, as the T_A had reached a magnitude sufficient to overcome the T_{Resist}.

Switching from SBs to EBs reduced the startup torque from 0.021 Nm to 0.01925 Nm. While this reduction reflects an improvement, it was notably smaller than the reductions achieved at lower U_∞, where the EBs had a more significant impact. Similarly, replacing the standard NACA0015 rotor with the optimized version decreased the startup torque from 0.021 Nm to 0.01925 Nm for the SB-DVAWT. This modest reduction suggests that at higher U_∞, the drag reduction effect becomes less pronounced, as the substantial T_A already overcomes other resisting forces with relative ease.

For the DVAWT featuring both EBs and the optimized NACA0015 rotor, the startup torque stabilized at 0.01925 Nm. This shows that at this U_∞, the combination of EBs and the modified airfoil reached an optimization point. The improvements in lift and drag reduction were fully realized, and further changes had little effect on the startup torque at this U_∞.

At a U_∞ of 9.50 m/s and a H of 35 cm, the DVAWT with EBs and the optimized NACA0015 rotor exhibit enhances in $T_{Self-starting}$ from 0.01225 Nm to 0.01925 Nm. This trend contrasts with the efficiency observed at lower U_∞. It suggests that at higher U_∞, the aerodynamic characteristics of the optimized rotor and EBs may reach a threshold, where increased drag starts to affect the startup torque, instead of continuing to reduce it. This outcome could result from the heightened sensitivity to F_D at higher velocities, which counteracts the lift benefits typically provided by the embossed surface and optimized airfoil.

Similarly, at $U_\infty = 10$ m/s, the startup torque increased from 0.00875 Nm to 0.0175 Nm when we used both the EBs and the optimized NACA0015 rotor. This trend indicates that, while the EB design is generally effective in reducing the torque required to overcome static friction—especially at lower U_∞—it becomes less efficient at higher U_∞. This may be due to the embossed material's tendency to enhance flow adherence at low-to-moderate U_∞, reducing static friction and aiding self-starting, but creating excess drag at higher U_∞.

As observed across U_∞ from 1 to 9 m/s, the DVAWT with EBs typically requires less $T_{Self-starting}$ at a H of 35 cm. Unlike SB-DVAWTs, which require additional torque to overcome static friction, the embossed surface design facilitates rotation initiation by effectively managing airflow adherence, making it a self-starting configuration capable of initiating motion at lower U_∞. These results suggest that, at this H, EB-DVAWTs demonstrate superior ability to overcome T_{Resist}, enabling effective self-starting even as conditions change.

Next, the performance is analyzed with an increased H of 75 cm to evaluate how higher blade positioning influences torque and self-starting efficiency at higher U_∞.

5.3.2. Comparing the torque required to start a DVAWT at a H of 75 cm

At a H of 75 cm, Fig. 12 shows the $T_{Self-starting}$ trends for both NACA0015 and NACA0015-Opt rotors with SB-DVAWT and EB-DVAWT across various U_∞. Compared to lower U_∞, DVAWTs exhibit poorer self-starting performance at minimal U_∞, resulting in a higher need for $T_{Self-starting}$. At low U_∞, the T_A is too low to overcome the static resisting torques (T_f, T_I, and T_D). However, as U_∞ increases, T_A also rises, allowing the DVAWTs to overcome these resisting forces more effectively. At a U_∞ of 0 m/s, no startup torque applies because no aerodynamic force acts to initiate rotation in any DVAWT configuration. This

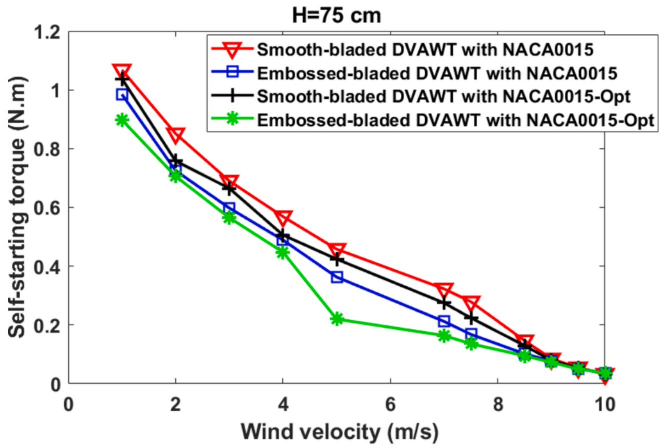

Fig. 12. Comparison of required $T_{Self-starting}$ at different U_∞ at a H of 75 cm.

starting point underscores that the initial requirement for $T_{Self-starting}$ fundamentally depends on the presence of wind flow.

At a U_∞ of 1 m/s and a H of 75 cm, the $T_{Self-starting}$ requirements differ significantly between EB-DVAWTs and those with SB-DVAWTs. DVAWTs equipped with EBs require less $T_{Self-starting}$ than their SB counterparts, with the modified NACA0015 rotor further reducing the required torque to 0.898 Nm. This configuration demonstrates superior self-starting capability due to enhanced aerodynamic characteristics, including increased lift and reduced drag.

The reduction in startup torque necessary for the EBs and modified airfoil configuration arises from the interaction between T_A and the opposing forces of T_f, T_I, and T_D. As U_∞ increases, T_A gains prominence, enabling it to counteract T_f, T_I, and T_D more efficiently. The EB design, combined with the modified NACA0015 rotor, enhances lift and reduces drag, directly increasing T_A. This improvement means the DVAWT requires less force to overcome static friction and initiate rotation, thereby reducing startup torque.

In SB-DVAWTs, the modified NACA0015 rotor also positively impacts startup torque requirements, though to a lesser extent than with EBs. This occurs because the optimized airfoil improves T_A by enhancing lift and reducing drag, although it does not match the aerodynamic adherence provided by the EBs. At a U_∞ of 2 m/s and a H of 75 cm, the $T_{Self-starting}$ required for each DVAWT was lower than the U_∞ of 1 m/s.

This trend shows that as U_∞ increases, T_A becomes more effective at countering resistive forces like T_f, T_I, and T_D, resulting in a lower overall $T_{Self-starting}$. The EB-DVAWT combined with the optimized NACA0015 rotor demonstrated the lowest startup torque requirements, achieving the best performance among all configurations. This improvement resulted from the combined benefits of the EB design and the optimized airfoil shape.

The EBs reduced drag and enhanced lift, leading to a higher T_A that more effectively overcame the resisting forces, making it easier for the DVAWT to initiate rotation. Moreover, replacing SBs with EBs reduced the required startup torque from 0.851 Nm (for the SB-DVAWT with NACA0015 configuration) to 0.725 Nm. This reduction stems from the superior aerodynamic characteristics of EBs, which reduce resistance to motion at low U_∞.

The modified NACA0015 rotor also helped lower the $T_{Self-starting}$ for the SB-DVAWT, bringing the torque requirement down from 0.851 Nm to 0.758 Nm. This improvement is due to the airfoil modification, which optimizes the C_L/C_D, reducing drag and increasing lift. As a result, the T_A increases, helping to overcome resistance and reducing the torque needed to initiate rotation.

At a U_∞ of 3 m/s, the $T_{Self-starting}$ required for each DVAWT configuration continued to decrease than the torque requirements at 2 m/s and 1 m/s. This decrease with increasing U_∞ highlights the positive effect of T_A, which becomes stronger as U_∞ rises, allowing it to more effectively counteract the T_{Resist}: T_f, T_I, and T_D. Among the DVAWT configurations, the EB-DVAWT utilizing the optimized NACA0015 rotor required the lowest $T_{Self-starting}$, demonstrating the advantages of both the EB design and the optimized airfoil shape. The EB texture helps reduce drag while increasing lift, leading to a more effective transformation of wind energy into rotational energy. This increased efficiency leads to a higher T_A, facilitating the operation of the DVAWT to surpass the initial resistance forces and initiate rotation.

In contrast, the SB-DVAWT utilizing the NACA0015 rotor indicated the greatest $T_{Self-starting}$ necessity at this U_∞. The SB surface combined with the standard airfoil shape produces a less favorable C_L/C_D, meaning more torque is needed to overcome the resisting forces. This configuration, therefore, struggles more with self-starting compared to the EB-DVAWT.

The improved performance of the optimized NACA0015 rotor is also evident here, as it enhances the lift characteristics while reducing drag, further decreasing the required startup torque for both SB-DVAWT and EB-DVAWT.

At a U_∞ of 4 m/s, the $T_{Self-starting}$ required for each DVAWT continued to follow the trend noticed at lower U_∞, with overall reductions as U_∞ increased. The EB-DVAWT configuration, which uses the optimized NACA0015-Opt rotor, showed the lowest $T_{Self-starting}$ requirement of 0.448 Nm.

This result highlights the aerodynamic benefits of the EB texture and the optimized airfoil shape, which enhance the C_L/C_D, thereby reducing the $T_{Self-starting}$.

The EBs are particularly effective at redistributing aerodynamic forces along the blade surface, minimizing localized stress points, and optimizing torque efficiency. This redistribution of forces also helps counteract the primary T_{Resist}, including T_f, T_I, and T_D, enabling the DVAWT to overcome static resistance with less initial torque. In contrast, the SB-DVAWT, utilizing the NACA0015 rotor, required the maximum self-starting torque of 0.569 Nm.

This configuration's higher $T_{Self-starting}$ results from the lack of optimized C_L properties and a higher C_D profile, which leads to inefficient transformation of wind energy into rotational energy, thus requiring more torque to initiate motion. The use of the optimized NACA0015-Opt rotor further reduces the required $T_{Self-starting}$ in both SB and EB DVAWTs configurations by improving lift and keeping drag levels low. This improvement in aerodynamic performance increases the T_A, which more effectively offsets the T_{Resist} as U_∞ rises, confirming the effectiveness of the modified airfoil and EB design at this higher U_∞.

At a U_∞ of 5 m/s, the $T_{Self-starting}$ requirement continued to decrease across all DVAWT configurations, consistent with the trend observed at lower U_∞. The EB-DVAWT utilized the optimized NACA0015-Opt rotor required the lowest $T_{Self-starting}$, measured at 0.22 Nm, highlighting the efficiency gains achieved by this combination.

The EB structure improves aerodynamic load distribution along the blade, minimizing stress concentrations and enhancing torque efficiency. This even load distribution reduces localized drag and more effectively counteracts initial inertia and T_f, leading to a lower overall $T_{Self-starting}$ requirement. In contrast, the SB-DVAWT utilizing the NACA0015 rotor required the greatest $T_{Self-starting}$, at 0.458 Nm. The SB surface, combined with the original NACA0015 rotor, is less effective at generating F_L and managing F_D, resulting in higher resistance to rotation. This configuration, therefore, requires more torque to initiate movement, especially at this higher U_∞, where aerodynamic improvements play a crucial role.

The modified NACA0015-Opt rotor consistently reduces the $T_{Self-starting}$ across configurations by improving lift and minimizing drag. This modification enhances the T_A, which more effectively counterbalances the T_{Resist}—including T_I and T_D—as the U_∞ increases.

At a U_∞ of 7 m/s, a clear trend emerges in the $T_{Self-starting}$ required by different DVAWT configurations, with each modification contributing distinctly to performance improvements. The SB-DVAWT utilizing the NACA0015 rotor had the greatest $T_{Self-starting}$ requirement, at 0.323 Nm.

Altering the NACA0015 rotor alone reduced this requirement to 0.275 Nm, demonstrating that the optimized airfoil shape effectively enhances lift and reduces drag, resulting in a modest reduction in starting torque.

Switching from SBs to EBs further reduced the required $T_{Self-starting}$ to 0.212 Nm. This improvement reflects the impact of the EB surface, which facilitates a more favorable distribution of aerodynamic loads across the blade. The embossed surface reduces drag-related T_{Resist} (T_D), allowing the T_A generated by the wind to counteract T_I and T_f more effectively.

Combining EBs with the modified NACA0015-Opt rotor achieved the most substantial reduction in $T_{Self-starting}$, lowering the required startup torque to 0.164 Nm. This configuration improves aerodynamic efficiency by increasing lift while reducing drag and overall resistance to rotation. At 7 m/s, the combined effect of the EB structure and the optimized airfoil shape results in superior self-starting performance, allowing the DVAWT to initiate rotation with minimal resistance.

At$U_\infty = 7.5$ m/s and 8.5 m/s, the DVAWT configurations required less startup torque as U_∞ increased. Among all configurations, the combination of EBs with the optimized NACA0015-Opt rotor demonstrated the lowest $T_{Self-starting}$ requirements across all U_∞ values from 1 m/s to 8.5 m/s, highlighting the efficiency of these changes in enhancing performance.

The EBs are especially effective in reducing startup torque, even more so than the airfoil modification by itself. By distributing aerodynamic loads more effectively and enhancing lift, the EBs reduce the torque needed to overcome resisting forces, including T_D and T_f, which hinder the DVAWT's initial rotation. Additionally, the altered NACA0015 rotor shape improves the C_L/C_D, reducing the startup torque for both SB-DVAWT and EB-DVAWT compared to the original airfoil setup. When combined with EBs, the modified NACA0015 rotor enhances aerodynamic performance by improving lift characteristics and reducing drag, which minimizes the T_I required for rotation.

At a U_∞ of 9 m/s, each DVAWT required less startup torque than at the previous, lower U_∞, indicating the continued influence of increased U_∞ in reducing initial resistance. Transitioning from SB-DVAWT to EB-DVAWT reduced the startup torque from 0.085 Nm to 0.079 Nm. Although this reduction was less substantial than that observed at lower U_∞, it suggests a diminishing effect of embossing as U_∞ increases. This more minor reduction may reflect the reduced incremental benefits of EBs on torque efficiency as aerodynamic forces become more dominant at higher U_∞.

Utilizing the modified NACA0015 rotor with SB-DVAWT at this U_∞ further lowered the startup torque requirement from 0.085 Nm to 0.079 Nm, matching the effect of switching to EBs alone. However, the combination of EBs with the altered NACA0015 rotor resulted in a startup torque of 0.073 Nm, which significantly improved over other configurations. The efficiency of this combination can be due to the optimized balance between C_L generation and C_D reduction, which allows the T_A to effectively counteract resisting forces such as T_f, T_D, and T_I, particularly during the initial moments of rotation.

At a U_∞ of 9.50 m/s, each DVAWT configuration demonstrated a decrease in $T_{Self-starting}$ compared to lower U_∞, following the trend observed in previous measurements. As U_∞ increases, the T_A becomes more significant, counteracting the resisting forces contributing to the required startup torque. In this case, T_A effectively offsets T_f, T_I, and T_D, resulting in a reduction in the overall startup torque.

Transitioning from SBs to EBs reduced the startup torque from 0.055 Nm to 0.053 Nm. Although the reduction was more minor compared to lower U_∞, it still reflects the impact of the EB design in decreasing drag and enhancing lift. The EBs generate less resistance than SBs, thus reducing the T_f and improving lift, which helps overcome T_I more effectively, particularly at higher U_∞.

Similarly, the modified NACA0015 rotor with SBs reduced the startup torque from 0.055 Nm to 0.053 Nm. The modified airfoil improves aerodynamic performance by optimizing the C_L/C_D, which lowers drag and reduces the T_{Resist}. The reduction in T_D enables the DVAWT to start more efficiently, particularly by decreasing resistance to initial motion.

The most significant reduction in startup torque occurred when combining the EBs with the modified NACA0015 rotor, bringing the torque requirement down to 0.050 Nm. This combination of design features optimizes the aerodynamic efficiency of the rotor. The EBs help reduce drag and improve lift, decreasing T_D and T_I, while the modified airfoil further enhances these effects by reducing drag and optimizing lift characteristics.

At a U_∞ of 10 m/s, unlike the trend seen at lower U_∞, switching from SBs to EBs led to an increase in $T_{Self-starting}$ for the DVAWT, rising from 0.033 Nm to 0.037 Nm. This increase suggests that, at higher U_∞, the embossed design may introduce additional drag, thereby raising aerodynamic resistance and increasing the T_D, which counteracts the anticipated improvement in the C_L/C_D and reduces self-starting efficiency.

Similarly, modifying the NACA0015 rotor for SBs resulted in a modest increase in the required starting torque, from 0.033 Nm to 0.034 Nm, indicating a noticeable, though slight, impact. This slight increase suggests that, at higher U_∞, the altered airfoil shape may create an additional aerodynamic load, which translates into increased T_D and T_I, which slightly elevate the torque needed to initiate motion.

For the EB-DVAWT, modifying the airfoil geometry did not result in a substantial change in $T_{Self-starting}$, as it remained at 0.037 Nm. This outcome suggests that the combined effect of the EBs and altered airfoil shape may yield diminishing returns at higher U_∞, where the drag characteristics outweigh the lift benefits. As a result, startup performance remained stable but did not improve, as the T_A was balanced by the T_D and T_I at this U_∞, preventing further reduction in $T_{Self-starting}$.

Su et al. [93] et al. studied an SB-DVAWT with three sets of blades and found it outperformed a conventional H-type rotor in terms of C_p across U_∞ from 4.54 m/s to 8.82 m/s.

Incrementing the H of the DVAWT from 35 cm to 75 cm resulted in a reduction of $T_{Self-starting}$ requirements for the EB-DVAWT compared to the SB-DVAWT, across U_∞ ranging from 9 m/s to 9.5 m/s. This enhancement allows the EB-DVAWT to achieve lower starting torque even at higher U_∞, up to 9.5 m/s, in contrast to the SB-DVAWT at 9 m/s. Several factors contribute to the improvement, including the reduced static friction during the initiation of rotation in the EBs.

The unique design of the EBs minimizes the resistance encountered at the start of the rotation, enabling a more efficient application of torque than SBs. In contrast, SBs experience higher static friction, requiring additional torque to overcome this resistance. Additionally, increasing the H also increases the surface area, which creates a larger contact area with the air, improving aerodynamic performance.

This enables more efficient energy conversion, further decreasing the $T_{Self-starting}$ requirement. The enhanced aerodynamic properties of the EBs, combined with the increased H, facilitate better airflow attachment, reducing drag and enhancing lift. These factors contribute to the decreased $T_{Self-starting}$ requirement for the EB-DVAWT, even at higher U_∞. Additionally, the decrease in $T_{Self-starting}$ can be attributed to better management of T_{Resist}, including T_f, T_I, and T_D.

The EBs reduce drag and increase lift, further aiding the DVAWT in overcoming these resisting forces with less effort. EB-DVAWTs are more efficient at converting wind energy into rotational energy, even at higher U_∞, while SB-DVAWTs need more torque to start rotating.

The higher H of 75 cm also allows for better distribution of aerodynamic forces along the blade, reducing localized stresses and improving torque efficiency. This is important for ensuring that the DVAWT operates efficiently at higher U_∞, where T_A plays a larger role in overcoming resistance forces. The combined effect of increased H and improved aerodynamic performance contributes to the lower starting torque requirement of the EB-DVAWT.

6. Conclusions and future work

This study focused on optimizing the aerodynamic performance of three rotors—NACA0015, NACA4412, and NACA4415—to improve the C_p of VAWTs at a Re_c of 45,192. Among the optimized airfoils, we selected NACA0015 for its superior C_p. Additionally, the research examined the $T_{Self-starting}$ performance of EB and SB at two H (35 cm and 75 cm) while optimizing the NACA0015 rotor. It further analyzed the impact of H variations on torque performance for both blade types, leading to the following results.

Modifying the NACA0015 rotor to the optimized NACA0015-Opt design led to a significant 14.45 % increase in peak C_p compared to the original NACA0015 rotor. This improvement illustrates the significant influence of airfoil optimization on the rotor's aerodynamic performance, enhancing its efficiency in converting wind energy into mechanical power.

The study also demonstrates that comparatively straightforward design modifications, such as optimizing the airfoil and rotor configurations, can lead to notable performance advancements, offering an effective method for enhancing the performance of DVAWTs across different U_∞ scenarios.

At a H of 35 cm, experimental results showed that at U_∞ of 1, 2, 3, 4, 5, 6, 7, 8, and 9 m/s:

– The EB-DVAWT with the NACA0015 rotor required 8.24 %, 10 %, 11.76 %, 11.65 %, 21.15 %, 32.5 %, 38.9 %, 30 %, and 8.33 % less $T_{Self-starting}$, respectively, compared to the baseline SB-DVAWT with the NACA0015 rotor.

– The SB-DVAWT with the NACA0015-Opt rotor required 2.06 %, 3.75 %, 2.94 %, 3.16 %, 7.69 %, 12.5 %, 16.67 %, 10 %, and 8.33 % less $T_{Self-starting}$, respectively, when compared to the baseline SB-DVAWT with the NACA0015 rotor.

– The EB-DVAWT with the NACA0015-Opt rotor required 14.43 %, 15 %, 16.17 %, 21.77 %, 34.06 %, 47.5 %, 50.01 %, 35.71 %, and 8.34 % less $T_{Self-starting}$, respectively, compared to the baseline SB-DVAWT with the NACA0015 rotor.

At a H of 75 cm, experimental results showed that at U_∞ of 1, 2, 3, 4, 5, 6, 7, 8, 9, and 9.5 m/s:

– The EB-DVAWT utilizing the NACA0015 rotor required 7.77 %, 14.81 %, 13.33 %, 14.05 %, 20.74 %, 34.38 %, 39.64 %, 30.61 %, 9.41 %, and 7.27 % less $T_{Self-starting}$, respectively, compared to the baseline SB-DVAWT with the NACA0015 rotor.

– The SB-DVAWT with the NACA0015-Opt rotor required 2.81 %, 10.93 %, 3.62 %, 11.06 %, 7.42 %, 14.85 %, 19.71 %, 11.56 %, 7.06 %, and 3.64 % less $T_{Self-starting}$, respectively, compared to the baseline SB-DVAWT with the NACA0015 rotor.

– The EB-DVAWT with the NACA0015-Opt rotor required 15.92 %, 17.04 %, 18.12 %, 21.23 %, 52.06 %, 49.23 %, 51.25 %, 35.2 %, 14.12 %, and 9.09 % less $T_{Self-starting}$, respectively, compared to the baseline SB-DVAWT with the NACA0015 rotor.

At H of 35 cm and 75 cm, the optimized EB-DVAWT exhibited significantly lower self-$T_{Self-starting}$ than other configurations, particularly at U_∞ ranging from 1 to 9.5 m/s. The optimized airfoil improved aerodynamic performance by reducing friction, inertia, and drag, while increasing lift. Increasing the H to 75 cm further enhanced performance by increasing the surface area exposed to the wind, which reduced drag and distributed aerodynamic forces more evenly. Together, the increased H and improved airfoil shape significantly reduced the $T_{Self-starting}$, making the DVAWT more efficient across a wider range of U_∞.

For future research, we propose replacing the SBs in DVAWTs with EBs, as the advancements discussed in this paper highlight the potential of this design. Priority will be placed on real-world assessments of self-starting performance for J-shaped VAWTs with EBs, as well as for hybrid Darrieus-Savonius VAWTs equipped with EBs. We will carry out these investigations in collaboration with Solar Turbine Arta Energy in Iran and ABSCUBE Engineering & Education in Australia. Furthermore, our ongoing study on EBs aims to enhance the $T_{Self-starting}$ of Darrieus vertical axis tidal turbines, underscoring the broader applicability of EB designs across both wind and water energy systems.

CRediT authorship contribution statement

Hossein Seifi Davari: Writing – original draft, Visualization, Validation, Software, Resources, Methodology, Investigation, Formal analysis, Data curation, Conceptualization, Funding acquisition. **Ruxandra Mihaela Botez:** Writing – review & editing, Validation, Supervision, Investigation, Conceptualization, Formal analysis, Methodology, Software. **Mohsen Seify Davari:** Writing – original draft, Visualization, Validation, Software, Resources, Methodology, Investigation, Formal analysis, Data curation, Conceptualization, Funding acquisition. **Harun Chowdhury:** Writing – review & editing, Supervision, Investigation, Software. **Hasan Hosseinzadeh:** Validation, Software, Formal analysis, Data curation.

Declaration of competing interest

The authors declare that they have no known competing financial interests or personal relationships that could have appeared to influence the work reported in this paper.

Data availability

Data will be made available on request.

References

[1] Abouemara K, Shahbaz M, Boulfrad S, McKay G, Al-Ansari T. Design of an integrated system that combines the steam gasification of plastic waste and a solid oxide fuel cell for sustainable power generation. Energy Convers Manage: X 2024;21:100524. https://doi.org/10.1016/j.ecmx.2024.100524.

[2] Ghasemi A, Rad HN, Izadyar N, Marefati M. Optimizing industrial energy: An eco-efficient system for integrated power, oxygen, and methanol production using coke plant waste heat and electrolysis. Energy Convers Manage: X 2024;22:100571. https://doi.org/10.1016/j.ecmx.2024.100571.

[3] Corigliano O, Algieri A. A comprehensive investigation on energy consumptions, impacts, and challenges of the food industry. Energy Convers Manage: X 2024;100661. https://doi.org/10.1016/j.ecmx.2024.100661.

[4] Malode SJ, Prabhu KK, Mascarenhas RJ, Shetti NP, Aminabhavi TM. Recent advances and viability in biofuel production. Energy Convers Manage: X 2021;10:100070. https://doi.org/10.1016/j.ecmx.2020.100070.

[5] Podkovalnikov S, Marchenko O, Trofimov L, Chudinova L, Solomin S, Trofimov I. Interstate power interconnection along with carbon dioxide emission constraint collaboration: Effective tool for low-carbon electric power expansion in Northeast Asia. Energy Convers Manage: X 2024;100639. https://doi.org/10.1016/j.ecmx.2024.100639.

[6] Ayodele OF, Ayodele BV, Mustapa SI, Fernando Y. Effect of activation function in modeling the nexus between carbon tax, CO2 emissions, and gas-fired power plant parameters. Energy Convers Manage: X 2021;12:100111. https://doi.org/10.1016/j.ecmx.2021.100111.

[7] Islam MA, Ali MN, Al Mamun A, Hossain MS, Maruf MH, Shihavuddin ASM. Optimizing energy solutions: A techno-economic analysis of solar-wind hybrid power generation in the coastal regions of Bangladesh. Energy Convers Manage: X 2024;22:100605. https://doi.org/10.1016/j.ecmx.2024.100605.

[8] Khan NR, Rashid AB. Carbon-based nanomaterials: A paradigm shift in biofuel synthesis and processing for a sustainable energy future. Energy Convers Manage: X 2024;100590. https://doi.org/10.1016/j.ecmx.2024.100590.

[9] Skorek-Osikowska A, Martín-Gamboa M, Dufour J. Thermodynamic, economic and environmental assessment of renewable natural gas production systems. Energy Convers Manage: X 2020;7:100046. https://doi.org/10.1016/j.ecmx.2020.100046.

[10] Voldsund M, Reyes-Lúa A, Fu C, Ditaranto M, Nekså P, Mazzetti MJ, et al. Low carbon power generation for offshore oil and gas production. Energy Convers Manage: X 2023;17:100347. https://doi.org/10.1016/j.ecmx.2023.100347.

[11] Hoseinzadeh S, Garcia DA. AI-driven innovations in greenhouse agriculture: Reanalysis of sustainability and energy efficiency impacts. Energy Convers Manage: X 2024;24:100701. https://doi.org/10.1016/j.ecmx.2024.100701.

[12] Ali MB, Altamimi A, Kazmi SAA, Khan ZA, Alyami S. Techno-economic-environmental optimization of on-grid hybrid renewable energy-electric vehicle

charging stations in BTS infrastructure. Energy Convers Manage: X 2024;100644. https://doi.org/10.1016/j.ecmx.2024.100644.
[13] Vávrová K, Knápek J, Weger J, Outrata D, Králík T. Complex aspects of climate change impacts on the cultivation of perennial energy crops in the Czech Republic. Energy Convers Manage: X 2023;20:100465. https://doi.org/10.1016/j.ecmx.2023.100465.
[14] Habour RM, Carton JG. Electricity system optimisation based on Python model for renewable electricity generation portfolio. Energy Convers Manage: X 2024;100771. https://doi.org/10.1016/j.ecmx.2024.100771.
[15] Onodera H, Delage R, Nakata T. Systematic effects of flexible power-to-X operation in a renewable energy system - A case study from Japan. Energy Convers Manage: X 2023;20:100416. https://doi.org/10.1016/j.ecmx.2023.100416.
[16] Hackenberg A, Kappertz L, Rapol S, Solovievskyi V, Büskens C. Optimal dimensioning of renewable energy generation and storage systems. Energy Convers Manage: X 2024;100773. https://doi.org/10.1016/j.ecmx.2024.100773.
[17] Hosseinifard F, Hosseinpour M, Salimi M, Amidpour M. Achieving net zero energy penalty in post-combustion carbon capture through solar energy: Parabolic trough and photovoltaic technologies. Energy Convers Manage: X 2024;100757. https://doi.org/10.1016/j.ecmx.2024.100757.
[18] Afonaa-Mensah S, Odoi-Yorke F, Majeed IB. Evaluating the impact of industrial loads on the performance of solar PV/diesel hybrid renewable energy systems for rural electrification in Ghana. Energy Convers Manage: X 2024;21:100525. https://doi.org/10.1016/j.ecmx.2024.100525.
[19] Jawad J, Hussain A, Mabrouk A. Pilot testing of water utilization for integrated solar energy storage and power production using linear Fresnel collector and organic Rankine cycle. Energy Convers Manage: X 2024;23:100625. https://doi.org/10.1016/j.ecmx.2024.100625.
[20] Álvaro AG, Palomar CR, Torre RM, Redondo DH, de Godos CI. Hybridization of anaerobic digestion with solar energy: A solution for isolated livestock farms. Energy Convers Manage: X 2023;20:100488. https://doi.org/10.1016/j.ecmx.2023.100488.
[21] Skiadopoulos A, Antonopoulou C, Atsonios K, Grammelis P, Gkountas A, Bakalis P, et al. Assessment of the Trilateral Flash Cycle potential for efficient solar energy conversion in Europe. Energy Convers Manage: X 2023;20:100432. https://doi.org/10.1016/j.ecmx.2023.100432.
[22] Sharma DK, Sharma D, Ali AH. Optimization and thermo-economic performance of a solar-powered vapor absorption cooling system integrated with sensible thermal energy storage. Energy Convers Manage: X 2023;20:100440. https://doi.org/10.1016/j.ecmx.2023.100440.
[23] Omgba BS, Lontsi F, Ndame MK, Olivier SMT, Mbue IN. Development and energy analysis of a solar-assisted air conditioning system for energy saving. Energy Convers Manage: X 2023;19:100390. https://doi.org/10.1016/j.ecmx.2023.100390.
[24] Kashan ME, Fung AS, Eisapour AH. Insulated concrete form foundation wall as solar thermal energy storage for Cold-Climate building heating system. Energy Convers Manage: X 2023;19:100391. https://doi.org/10.1016/j.ecmx.2023.100391.
[25] Eltayeb WA, Somlal J, Kumar S, Rao SK. Design and analysis of a solar-wind hybrid renewable energy tree. Results Eng 2023;17:100958. https://doi.org/10.1016/j.rineng.2023.100958.
[26] Al-Buraiki AS, Al-Sharafi A, Yilbas BS, Al-Merbati AS, Kassas M. Influence of load coordination with solar energy potential on the optimal sizing of standalone PV systems. Energy Convers Manage: X 2023;17:100343. https://doi.org/10.1016/j.ecmx.2022.100343.
[27] Thinsurat K, Ma Z, Roskilly AP, Bao H. Compressor-assisted thermochemical sorption integrated with solar photovoltaic-thermal collector for seasonal solar thermal energy storage. Energy Convers Manage: X 2022;15:100248. https://doi.org/10.1016/j.ecmx.2022.100248.
[28] Eltayeb W, Yedukondalu G, Srinath A. Design and development of a cleaning robot for solar panels with sun tracking. Journal of Green Engineering 2020;10(10):9517–32.
[29] Mohebi P, Roshandel R. Optimal design and operation of solar energy system with heat storage for agricultural greenhouse heating. Energy Convers Manage: X 2023;18:100353. https://doi.org/10.1016/j.ecmx.2023.100353.
[30] Jamali R, Sohani A, Hemmatpour K, Behrang M, Ghobeity A. Experimental study of pressure pulsation in a large-scale hydropower plant with Francis turbine units and a common penstock. Energy Convers Manage: X 2022;16:100308. https://doi.org/10.1016/j.ecmx.2022.100308.
[31] Jovan DJ, Dolanc G, Pregelj B. Cogeneration of green hydrogen in a cascade hydropower plant. Energy Convers Manage: X 2021;10:100081. https://doi.org/10.1016/j.ecmx.2021.100081.
[32] Shanegowda TG, Shashikumar CM, Gumtapure V, Madav V. Comprehensive analysis of blade geometry effects on Savonius hydrokinetic turbine efficiency: Pathways to clean energy. Energy Convers Manage: X 2024;100762. https://doi.org/10.1016/j.ecmx.2024.100762.
[33] Skiarski A, Faedo N, Ringwood JV. Optimisation and control of tidal range power plants operation: Is there scope for further improvement? Energy Convers Manage: X 2024;100657. https://doi.org/10.1016/j.ecmx.2024.100657.
[34] Mehdipour H, Amini E, Naeeni STO, Neshat M, Gandomi AH. Optimization of power take-off system settings and regional site selection procedure for a wave energy converter. Energy Convers Manage: X 2024;22:100559. https://doi.org/10.1016/j.ecmx.2024.100559.
[35] Irshad AS, Zakir MN, Rashad SS, Lotfy ME, Mikhaylov A, Elkholy MH, et al. Comparative analyses and optimizations of hybrid biomass and solar energy systems based upon a variety of biomass technologies. Energy Convers Manage: X 2024;100640. https://doi.org/10.1016/j.ecmx.2024.100640.
[36] Permana DI, Fagioli F, De Lucia M, Rusirawan D, Farkas I. Energy, exergy, environmental and economy (4E) analysis of the existing biomass-ORC plant with capacity 150 kWe: A case study. Energy Convers Manage: X 2024;100646. https://doi.org/10.1016/j.ecmx.2024.100646.
[37] Merzic A, Turkovic N, Ikanovic N, Lapandic E, Kazagic A, Music M. Towards just transition of coal regions-Cultivation of short rotation coppices and dedicated energy crops for biomass co-firing vs photovoltaic power plants. Energy Convers Manage: X 2022;15:100267. https://doi.org/10.1016/j.ecmx.2022.100267.
[38] Bongomin O, Nzila C, Mwasiagi JI, Maube O. Comprehensive thermal properties, kinetic, and thermodynamic analyses of biomass wastes pyrolysis via TGA and Coats-Redfern methodologies. Energy Convers Manage: X 2024;24:100723. https://doi.org/10.1016/j.ecmx.2024.100723.
[39] Timilsina MS, Chaudhary Y, Bhattarai P, Uprety B, Khatiwada D. Optimizing pyrolysis and co-pyrolysis of plastic and biomass using Artificial Intelligence. Energy Convers Manage: X 2024;100783. https://doi.org/10.1016/j.ecmx.2024.100783.
[40] Sadeghi A, Maleki A, Haghighat S. Techno-economic analysis and optimization of a hybrid solar-wind-biomass-battery framework for the electrification of a remote area: A case study. Energy Convers Manage: X 2024;100732. https://doi.org/10.1016/j.ecmx.2024.100732.
[41] Gilani H, Sahebi H. Optimizing sustainable multiple biomass-to-biofuel conversion network with integrated water resource management utilizing data-driven robust planning. Energy Convers Manage: X 2024;24:100727. https://doi.org/10.1016/j.ecmx.2024.100727.
[42] Caligiuri C, Renzi M, Antolini D, Patuzzi F, Baratieri M. Optimizing the use of forestry biomass producer gas in dual fuel engines: A novel emissions reduction strategy for a micro-CHP system. Energy Convers Manage: X 2023;20:100498. https://doi.org/10.1016/j.ecmx.2023.100498.
[43] Oyekale J, Petrollese M, Cocco D, Cau G. Annualized exergoenvironmental comparison of solar-only and hybrid solar-biomass heat interactions with an organic Rankine cycle power plant. Energy Convers Manage: X 2022;15:100229. https://doi.org/10.1016/j.ecmx.2022.100229.
[44] Facci M, di Sipio E, Gola G, Montegrossi G, Galgaro A. Sustainable reuse of oil and gas wells for geothermal energy production: Numerical analysis of deep closed loop solutions in Italy. Energy Convers Manage: X 2024;100743. https://doi.org/10.1016/j.ecmx.2024.100743.
[45] Mohammadi MH, Abbasi HR, Ghodrat M. Optimal design of a hybrid thermal-and membrane-based desalination unit based on renewable geothermal energy. Energy Convers Manage: X 2021;12:100124. https://doi.org/10.1016/j.ecmx.2021.100124.
[46] Gabrielli P, Acquilino A, Siri S, Bracco S, Sansavini G, Mazzotti M. Optimization of low-carbon multi-energy systems with seasonal geothermal energy storage: The Anergy Grid of ETH Zurich. Energy Convers Manage: X 2020;8:100052. https://doi.org/10.1016/j.ecmx.2020.100052.
[47] Shaghaghi A, Honarvar F, Jafari M, Solati A, Zahedi R, Taghitahoone M. Thermodynamic and thermoeconomic evaluation of integrated hybrid solar and geothermal power generation cycle. Energy Convers Manage: X 2024;23:100685. https://doi.org/10.1016/j.ecmx.2024.100685.
[48] Shumiye WB, Ancha VR, Tadese AK, Zeru BA. Exergy analysis of solar-geothermal based power plant integrated with boiling, and reverse osmosis water purification. Energy Convers Manage: X 2022;15:100255. https://doi.org/10.1016/j.ecmx.2022.100255.
[49] Yang X, Tao Y, Jin Y, Ye B, Ye F, Duan W, et al. Time resolution of wind speed data introduces errors in wind power density assessment. Energy Convers Manage: X 2024;100753. https://doi.org/10.1016/j.ecmx.2024.100753.
[50] Eltayeb WA, Somlal J. Performance Enhancement of Darrieus Wind Turbines Using Plain Flap and Gurney Flap Configurations: A CFD Analysis. Results. Engineering 2024;103400. https://doi.org/10.1016/j.rineng.2024.103400.
[51] Boyle J, Littler T, Foley AM. Aggregator control of battery energy storage in wind power stations to maximize availability of regulation service. Energy Convers Manage: X 2024;24:100703. https://doi.org/10.1016/j.ecmx.2024.100703.
[52] Ding JW, Fu YS, Hsieh IYL. The cost of green: Analyzing the economic feasibility of hydrogen production from offshore wind power. Energy Convers Manage: X 2024;100770. https://doi.org/10.1016/j.ecmx.2024.100770.
[53] Wu J, Li S, Vasquez JC, Guerrero JM. A Bi-level Mode Decomposition Framework for Multi-step Wind Power Forecasting using Deep Neural Network. Energy Convers Manage: X 2024;100650. https://doi.org/10.1016/j.ecmx.2024.100650.
[54] Moradian S, Gharbia S, Iglesias G, Olbert AI. A copula post-processing method for wind power projections under climate change. Energy Convers Manage: X 2024;23:100660. https://doi.org/10.1016/j.ecmx.2024.100660.
[55] Wang J, Cai S, Chen R, Tu Z, Li S. Operation strategy optimization of an integrated proton exchange membrane water electrolyzer and batch reverse osmosis desalination system powered by offgrid wind energy. Energy Convers Manage: X 2024;22:100607. https://doi.org/10.1016/j.ecmx.2024.100607.
[56] Al-Sharafi A, Al-Buraiki AS, Al-Sulaiman F, Antar MA. Hydrogen refueling stations powered by hybrid PV/wind renewable energy systems: Techno-socio-economic assessment. Energy Convers Manage: X 2024;22:100584. https://doi.org/10.1016/j.ecmx.2024.100584.
[57] Odoi-Yorke F, Adu TF, Ampimah BC, Atepor L. Techno-economic assessment of a utility-scale wind power plant in Ghana. Energy Convers Manage: X 2023;18:100375. https://doi.org/10.1016/j.ecmx.2023.100375.
[58] Mulumba AN, Farzaneh H. Techno-economic analysis and dynamic power simulation of a hybrid solar-wind-battery-flywheel system for off-grid power

supply in remote areas in Kenya. Energy Convers Manage: X 2023;18:100381. https://doi.org/10.1016/j.ecmx.2023.100381.
[59] Eikeland OF, Hovem FD, Olsen TE, Chiesa M, Bianchi FM. Probabilistic forecasts of wind power generation in regions with complex topography using deep learning methods: An Arctic case. Energy Convers Manage: X 2022;15:100239. https://doi.org/10.1016/j.ecmx.2022.100239.
[60] Simpson JG, Loth E. Super-rated operational concept for increased wind turbine power with energy storage. Energy Convers Manage: X 2022;14:100194. https://doi.org/10.1016/j.ecmx.2022.100194.
[61] Serat Z, Danishmal M, Mohammadi FM. Optimizing hybrid PV/wind and grid systems for sustainable energy solutions at the university campus: Economic, environmental, and sensitivity analysis. Energy Convers Manage: X 2024;24:100691. https://doi.org/10.1016/j.ecmx.2024.100691.
[62] Yousefi H, Moradi S, Zahedi R, Ranjbar Z. Developed analytic hierarchy process and multi criteria decision support system for wind farm site selection using GIS: A regional-scale application with environmental responsibility. Energy Convers Manage: X 2024;22:100594. https://doi.org/10.1016/j.ecmx.2024.100594.
[63] Calautit K, Johnstone C. State-of-the-art review of micro to small-scale wind energy harvesting technologies for building integration. Energy Convers Manage: X 2023;100457. https://doi.org/10.1016/j.ecmx.2023.100457.
[64] Wang Z, Dong B, Wang Y, Li M, Liu H, Han F. Analysis and evaluation of fuel cell technologies for sustainable ship power: Energy efficiency and environmental impact. Energy Convers Manage: X 2024;21:100482. https://doi.org/10.1016/j.ecmx.2023.100482.
[65] Islam MA, Ali MN, Mollick T, Islam A, Benitez IB, Habib SS, et al. Assessing the feasibility and quality performance of a renewable Energy-Based hybrid microgrid for electrification of remote communities. Energy Convers Manage: X 2024;23:100674. https://doi.org/10.1016/j.ecmx.2024.100674.
[66] ElFar OA, Chang CK, Leong HY, Peter AP, Chew KW, Show PL. Prospects of Industry 5.0 in algae: Customization of production and new advance technology for clean bioenergy generation. Energy Convers Manage: X 2021;10:100048. https://doi.org/10.1016/j.ecmx.2020.100048.
[67] Kabir KM, Binzaid S. Innovation of sustainable energy generating from lightweight vehicle applications. Energy Convers Manage: X 2024;22:100595. https://doi.org/10.1016/j.ecmx.2024.100595.
[68] Garcia DA, Raskovic P, Duić N. Technologies and strategies fostering the sustainable development of energy, water and environment systems. Energy Convers Manage: X 2024;100736. https://doi.org/10.1016/j.ecmx.2024.100736.
[69] Srivastava RK, Boddula R, Pothu R. Microbial fuel cells: Technologically advanced devices and approach for sustainable/renewable energy development. Energy Convers Manage: X 2022;13:100160. https://doi.org/10.1016/j.ecmx.2021.100160.
[70] Desta M, Lee T, Wu H. Life cycle energy consumption and environmental assessment for utilizing biofuels in the development of a sustainable transportation system in Ethiopia. Energy Convers Manage: X 2022;13:100144. https://doi.org/10.1016/j.ecmx.2021.100144.
[71] Tumma A, Dujjanutat P, Muanruksa P, Winterburn J, Kaewkannetra P. Biocircular platform for renewable energy production: Valorization of waste cooking oil mixed with agricultural wastes into biosolid fuels. Energy Convers Manage: X 2022;15:100235. https://doi.org/10.1016/j.ecmx.2022.100235.
[72] von Krauland AK, Long Q, Enevoldsen P, Jacobson MZ. United States offshore wind energy atlas: availability, potential, and economic insights based on wind speeds at different altitudes and thresholds and policy-informed exclusions. Energy Convers Manage: X 2023;20:100410. https://doi.org/10.1016/j.ecmx.2023.100410.
[73] Icaza-Alvarez D, Jurado F, Tostado-Véliz M, Arevalo P. Design to include a wind turbine and socio-techno-economic analysis of an isolated airplane-type organic building based on a photovoltaic/hydrokinetic/battery. Energy Convers Manage: X 2022;14:100202. https://doi.org/10.1016/j.ecmx.2022.100202.
[74] Rusu L. An evaluation of the synergy between the wave and wind energy along the west Iberian nearshore. Energy Convers Manage: X 2023;20:100453. https://doi.org/10.1016/j.ecmx.2023.100453.
[75] Akhter MZ, Ali AR, Jawahar HK, Omar FK, Elnajjar E. Enhanced energy extraction in small-scale wind turbines through slot-based passive blowing. Energy Convers Manage: X 2023;19:100400. https://doi.org/10.1016/j.ecmx.2023.100400.
[76] Hoxha B, Shesho IK, Filkoski RV. Optimization of wind farm layout to maximize the energy yield. Energy Convers Manage: X 2024;24:100700. https://doi.org/10.1016/j.ecmx.2024.100700.
[77] Li N, Zhou Y, Luo Q, Huang H. Discrete complex-valued code pathfinder algorithm for wind farm layout optimization problem. Energy Convers Manage: X 2022;16:100307. https://doi.org/10.1016/j.ecmx.2022.100307.
[78] Taoufik M, Fekri A. GIS-based multi-criteria analysis of offshore wind farm development in Morocco. Energy Convers Manage: X 2021;11:100103. https://doi.org/10.1016/j.ecmx.2021.100103.
[79] Chisale SW, Lee HS. Comprehensive onshore wind energy assessment in Malawi based on the WRF downscaling with ERA5 reanalysis data, optimal site selection, and energy production. Energy Convers Manage: X 2024;22:100608. https://doi.org/10.1016/j.ecmx.2024.100608.
[80] Khedr A, Castellani F. Critical issues in the moving reference frame CFD simulation of small horizontal axis wind turbines. Energy Convers Manage: X 2024;22:100551. https://doi.org/10.1016/j.ecmx.2024.100551.
[81] Ogrodnik N, Sudasinghe A, Heiber E, abo el Ella H, Fereidooni A, Matida E, Kaya T.. Pseudo three-dimensional numerical investigation of legacy vertical axis wind turbine configurations. Energy Convers Manage: X 2023;17:100338. https://doi.org/10.1016/j.ecmx.2022.100338.
[82] Ismail KA, Lino FA, de Almeida O, Teggar M, Scalon VL, Okita WM. Review on Small Horizontal-Axis Wind Turbines. Arab J Sci Eng 2024;49(2):1367–91. https://doi.org/10.1007/s13369-023-08314-6.
[83] Zhang H, Wen J, Zhan J, Xin D. Effects of blade number on the aerodynamic performance and wake characteristics of a small horizontal-axis wind turbine. Energ Conver Manage 2022;273:116410. https://doi.org/10.1016/j.enconman.2022.116410.
[84] Roga S, Bardhan S, Kumar Y, Dubey SK. Recent technology and challenges of wind energy generation: A review. Sustainable Energy Technol Assess 2022;52:102239. https://doi.org/10.1016/j.seta.2022.102239.
[85] Zhao Z, Wang D, Wang T, Shen W, Liu H, Chen M. A review: Approaches for aerodynamic performance improvement of lift-type vertical axis wind turbine. Sustainable Energy Technol Assess 2022;49:101789. https://doi.org/10.1016/j.seta.2021.101789.
[86] Azadani LN. Vertical axis wind turbines in cluster configurations. Ocean Eng 2023;272:113855. https://doi.org/10.1016/j.oceaneng.2023.113855.
[87] Gemayel D, Abdelwahab M, Ghazal T, Aboshosha H. Modelling of vertical axis wind turbine using large eddy simulations. Results Eng 2023;18:101226. https://doi.org/10.1016/j.rineng.2023.101226.
[88] Cuevas-Carvajal N, Cortes-Ramirez JS, Norato JA, Hernandez C, Montoya-Vallejo MF. Effect of geometrical parameters on the performance of conventional Savonius VAWT: A review. Renew Sustain Energy Rev 2022;161:112314. https://doi.org/10.1016/j.rser.2022.112314.
[89] Huang H, Luo J, Li G. Study on the optimal design of vertical axis wind turbine with novel variable solidity type for self-starting capability and aerodynamic performance. Energy 2023;271:127031. https://doi.org/10.1016/j.energy.2023.127031.
[90] Dominy R, Lunt P, Bickerdyke A, Dominy J. Self-starting capability of a Darrieus turbine. Proceedings of the Institution of Mechanical Engineers, Part A: Journal of Power and Energy. 2007;221(1):111-120. https://doi.org/10.1243/09576509JPE340.
[91] Sun SY, Liu HJ, Peng HY. Power performance and self-starting features of H-rotor and helical vertical axis wind turbines with different airfoils in turbulence. Energ Conver Manage 2023;292:117405. https://doi.org/10.1016/j.enconman.2023.117405.
[92] Douak M, Aouachria Z, Rabehi R, Allam N. Wind energy systems: Analysis of the self-starting physics of vertical axis wind turbine. Renew Sustain Energy Rev 2018;81:1602–10. https://doi.org/10.1016/j.rser.2017.05.238.
[93] Su H, Dou B, Qu T, Zeng P, Lei L. Experimental investigation of a novel vertical axis wind turbine with pitching and self-starting function. Energ Conver Manage 2020;217:113012. https://doi.org/10.1016/j.enconman.2020.113012.
[94] Shah OR, Jamal MA, Khan TI, Qazi UW. Experimental and numerical evaluation of performance of a variable pitch vertical-axis wind turbine. J Energy Res Technol 2022;144(6):061303. https://doi.org/10.1115/1.4051896.
[95] Hosseini A, Goudarzi N. Design and CFD study of a hybrid vertical-axis wind turbine by employing a combined Bach-type and H-Darrieus rotor systems. Energy Convers Manag 2019;189:49–59. https://doi.org/10.1016/j.enconman.2019.03.068.
[96] Chegini S, Asadbeigi M, Ghafoorian F, Mehrpooya M. An investigation into the self-starting of Darrieus-Savonius hybrid wind turbine and performance enhancement through innovative deflectors: A CFD approach. Ocean Eng 2023;287:115910. https://doi.org/10.1016/j.oceaneng.2023.115910.
[97] Yosry AG, Fernández-Jiménez A, Álvarez-Álvarez E, Marigorta EB. Design and characterization of a vertical-axis micro tidal turbine for low velocity scenarios. Energ Conver Manage 2021;237:114144. https://doi.org/10.1016/j.enconman.2021.114144.
[98] Moghimi M, Motawej H. Developed DMST model for performance analysis and parametric evaluation of Gorlov vertical axis wind turbines. Sustainable Energy Technol Assess 2020;37:100616. https://doi.org/10.1016/j.seta.2019.100616.
[99] Tavallaeinejad M, Fereidooni A, Païdoussis MP, Grewal A, Wickramasinghe V. An application of cantilevered plates subjected to extremely large amplitude deformations: A self-starting mechanism for vertical axis wind turbines. J Fluids Struct 2022;113:103666. https://doi.org/10.1016/j.jfluidstructs.2022.103666.
[100] Farzadi R, Bazargan M. 3D numerical simulation of the Darrieus vertical axis wind turbine with J-type and straight blades under various operating conditions including self-starting mode. Energy 2023;278:128040. https://doi.org/10.1016/j.energy.2023.128040.
[101] Abdolahifar A, Azizi M, Zanj A. Flow structure and performance analysis of Darrieus vertical axis turbines with swept blades: A critical case study on V-shaped blades. Ocean Eng 2023;280:114857. https://doi.org/10.1016/j.oceaneng.2023.114857.
[102] Howell R, Qin N, Edwards J, Durrani N. Wind tunnel and numerical study of a small vertical axis wind turbine. Renew Energy 2010;35(2):412–22. https://doi.org/10.1016/j.renene.2009.07.025.
[103] Keskin S, Ilbas M, Genc MS, Karasu I. Performance analysis of roughness-controlled vertical axis wind turbine. In AIAA AVIATION FORUM AND ASCEND 2024;4613. https://doi.org/10.2514/6.2024-4613.
[104] Tanürün HE, Akın AG, Acır A, Şahin İ. Experimental and Numerical Investigation of Roughness Structure in Wind Turbine Airfoil at Low Reynolds Number. Int J Thermodyn 2024;27(3):26–36. https://doi.org/10.5541/ijot.1455513.
[105] Hansen KL, Kelso RM, Dally BB. Performance variations of leading-edge tubercles for distinct airfoil profiles. AIAA J 2011;49(1):185–94. https://doi.org/10.2514/1.J050631.
[106] Gonçalves AN, Pereira JM, Sousa JM. Passive control of dynamic stall in a H-Darrieus Vertical Axis Wind Turbine using blade leading-edge protuberances.

Appl Energy 2022;324:119700. https://doi.org/10.1016/j.apenergy.2022.119700.

[107] Zamani M, Sangtarash A, Maghrebi MJ. Numerical study of porous media effect on the blade surface of vertical axis wind turbine for enhancement of aerodynamic performance. Energ Conver Manage 2021;245:114598. https://doi.org/10.1016/j.enconman.2021.114598.

[108] Tirandaz MR, Rezaeiha A. Effect of airfoil shape on power performance of vertical axis wind turbines in dynamic stall: Symmetric airfoils. Renew Energy 2021;173:422–41. https://doi.org/10.1016/j.renene.2021.03.142.

[109] Bachant P, Wosnik M. Effects of Reynolds number on the energy conversion and near-wake dynamics of a high solidity Vertical-Axis cross-flow turbine. Energies 2016;9(2):73. https://doi.org/10.3390/en9020073.

[110] Miller MA, Duvvuri S, Brownstein I, Lee M, Dabiri JO, Hultmark M. Vertical-axis wind turbine experiments at full dynamic similarity. J Fluid Mech 2018;844:707–20. https://doi.org/10.1017/jfm.2018.197.

[111] Peng YX, Xu YL, Zhu S, Li C. High-solidity straight-bladed vertical axis wind turbine: Numerical simulation and validation. J Wind Eng Ind Aerodyn 2019;193:103960. https://doi.org/10.1016/j.jweia.2019.103960.

[112] Maeda T, Kamada Y, Shimizu K, Ogasawara T, Nakai A, Kasuya T. Effect of rotor aspect ratio and solidity on a straight-bladed vertical axis wind turbine in three-dimensional analysis by the panel method. Energy 2017;121:1–9. https://doi.org/10.1016/j.energy.2016.12.112.

[113] Brusca S, Lanzafame R, Messina M. Design of a vertical-axis wind turbine: how the aspect ratio affects the turbine's performance. Int J Energy Environ Eng 2014;5:333–40. https://doi.org/10.1007/s40095-014-0129-x.

[114] Tong G, Yang S, Li Y, Feng F. Effects of blade tip flow on aerodynamic characteristics of straight-bladed vertical axis wind turbines. Energy 2023;283:129105. https://doi.org/10.1016/j.energy.2023.129105.

[115] Peng HY, Lam HF, Liu HJ. Power performance assessment of H-rotor vertical axis wind turbines with different aspect ratios in turbulent flows via experiments. Energy 2019;173:121–32. https://doi.org/10.1016/j.energy.2019.01.140.

[116] Wu YK, Lin HJ, Lin JH. Certification and testing technology for small vertical axis wind turbine in Taiwan. Sustainable Energy Technol Assess 2019;31:34–42. https://doi.org/10.1016/j.seta.2018.11.005.

[117] Wang WC, Wang JJ, Chong WT. The effects of unsteady wind on the performances of a newly developed cross-axis wind turbine: A wind tunnel study. Renew Energy 2019;131:644–59. https://doi.org/10.1016/j.renene.2018.07.061.

[118] Al-Ghriybah M, Zulkafli MF, Didane DH, Mohd S. The effect of inner blade position on the performance of the Savonius rotor. Sustainable Energy Technol Assess 2019;36:100534. https://doi.org/10.1016/j.seta.2019.100534.

[119] Franchina N, Persico G, Savini M. 2D–3D computations of a vertical axis wind turbine flow field: Modeling issues and physical interpretations. Renew Energy 2019;136:1170–89. https://doi.org/10.1016/j.renene.2018.09.086.

[120] Didane DH, Rosly N, Zulkafli MF, Shamsudin SS. Numerical investigation of a novel contra-rotating vertical axis wind turbine. Sustainable Energy Technol Assess 2019;31:43–53. https://doi.org/10.1016/j.seta.2018.11.006.

[121] Bedon G, Castelli MR, Benini E. Proposal for an innovative chord distribution in the Troposkien vertical axis wind turbine concept. Energy 2014;66:689–98. https://doi.org/10.1016/j.energy.2014.01.004.

[122] Balduzzi F, Drofelnik J, Bianchini A, Ferrara G, Ferrari L, Campobasso MS. Darrieus wind turbine blade unsteady aerodynamics: a three-dimensional Navier-Stokes CFD assessment. Energy 2017;128:550–63. https://doi.org/10.1016/j.energy.2017.04.017.

[123] Peng YX, Xu YL, Zhan S. A hybrid DMST model for pitch optimization and performance assessment of high-solidity straight-bladed vertical axis wind turbines. Appl Energy 2019;250:215–28. https://doi.org/10.1016/j.apenergy.2019.04.127.

[124] Bangga G, Dessoky A, Lutz T, Krämer E. Improved double-multiple-streamtube approach for H-Darrieus vertical axis wind turbine computations. Energy 2019;182:673–88. https://doi.org/10.1016/j.energy.2019.06.083.

[125] Tahani M, Babayan N, Mehrnia S, Shadmehri M. A novel heuristic method for optimization of straight blade vertical axis wind turbine. Energ Conver Manage 2016;127:461–76. https://doi.org/10.1016/j.enconman.2016.08.094.

[126] Pratumnopharat P, Leung PS. Validation of various windmill brake state models used by blade element momentum calculation. Renew Energy 2011;36(11):3222–7. https://doi.org/10.1016/j.renene.2011.03.027.

[127] Dyachuk E, Goude A. Simulating dynamic stall effects for vertical axis wind turbines applying a double multiple streamtube model. Energies 2015;8(2):1353–72. https://doi.org/10.3390/en8021353.

[128] Wendler R, Calderón-Muñoz WR, LeBoeuf R. Energy-based iteration scheme of the double-multiple streamtube model in vertical-axis wind turbines. Acta Mechanica 2016;227(11):3295–303. https://doi.org/10.1007/s00707-015-1544-7.

[129] Paraschivoiu I. Wind turbine design: with emphasis on Darrieus concept. Presses Inter Polytechnique 2002.

[130] Soraghan CE, Leithead WE, Feuchtwang J, Yue H. Double multiple streamtube model for variable pitch vertical axis wind turbines. 31st AIAA Appl Aerodyn Conf 2013;2802. https://doi.org/10.2514/6.2013-2802.

[131] Ghiasi P, Najafi G, Ghobadian B, Jafari A, Mazlan M. Analytical study of the impact of solidity, chord length, number of blades, aspect ratio and airfoil type on h-rotor darrieus wind turbine performance at low reynolds number. Sustainability 2022;14(5):2623. https://doi.org/10.3390/su14052623.

[132] Elkhoury M, Kiwata T, Aoun E. Experimental and numerical investigation of a three-dimensional vertical-axis wind turbine with variable-pitch. J Wind Eng Ind Aerodyn 2015;139:111–23. https://doi.org/10.1016/j.jweia.2015.01.004.

[133] Li S, Li Y. Numerical study on the performance effect of solidity on the straightbladed vertical axis wind turbine. In: Proceedings of Asia-Pacific Powerand Energy Engineering Conference (APPEEC), IEEE; 2010. p. 1–4. https://doi.org/10.1109/APPEEC.2010.5449269.

[134] Mohamed MH. Impacts of solidity and hybrid system in small wind turbines performance. Energy 2013;57:495–504. https://doi.org/10.1016/j.energy.2013.06.004.

[135] Maeda T, Kamada Y, Murata J, Furukawa K, Yamamoto M. Effect of number of blades on aerodynamic forces on a straight-bladed Vertical Axis Wind Turbine. Energy 2015;90:784–95. https://doi.org/10.1016/j.energy.2015.07.115.

[136] Paraschivoiu L. Aerodynamic loads and performance of the Darrieus rotor. Journal of Energy 1982;6(6):406–12. https://doi.org/10.2514/3.62621.

[137] Batista NC, Melício R, Mendes VMF, Calderón M, Ramiro A. On a self-start Darrieus wind turbine: Blade design and field tests. Renew Sustain Energy Rev 2015;52:508–22. https://doi.org/10.1016/j.rser.2015.07.147.

[138] Islam M, Ting DSK, Fartaj A. Aerodynamic models for Darrieus-type straight-bladed vertical axis wind turbines. Renew Sustain Energy Rev 2008;12(4):1087–109. https://doi.org/10.1016/j.rser.2006.10.023.

[139] Sheldahl RE. Aerodynamic characteristics of seven airfoil sections through 180 degrees angle of attack for use in aerodynamic analysis of vertical axis wind turbines. SAND80-2114 1981.

[140] Roh SC, Kang SH. Effects of a blade profile, the Reynolds number, and the solidity on the performance of a straight bladed vertical axis wind turbine. J Mech Sci Technol 2013;27(11):3299–307. https://doi.org/10.1007/s12206-013-0852-x.

[141] Subramanian A, Yogesh SA, Sivanandan H, Giri A, Vasudevan M, Mugundhan V, et al. Effect of airfoil and solidity on performance of small scale vertical axis wind turbine using three dimensional CFD model. Energy 2017;133:179–90. https://doi.org/10.1016/j.energy.2017.05.118.

[142] Zhang Y, Guo Z, Zhu X, Li Y, Song X, Cai C, et al. Investigation of aerodynamic forces and flow field of an H-type vertical axis wind turbine based on bionic airfoil. Energy 2022;242:122999. https://doi.org/10.1016/j.energy.2021.122999.

[143] Abul-Ela MS, Sayed AI, Elrefaei MEF. Performance comparative study of low Reynolds number airfoils utilized in vertical-axis wind turbines. Journal of Al-Azhar University Engineering Sector 2024;19(72):147–61. https://doi.org/10.21608/auej.2024.257724.1548.

[144] Abotaleb B, Takeyeldein MM, Huzayyin O, Elhadidi B. Impact of Negative Camber for Performance of Vertical Axis Wind Turbine 2024. https://doi.org/10.5109/7172281.

[145] Korukçu MÖ. Impact of Blade Modifications on the Performance of a Darrieus Wind Turbine. Processes 2024;12(4):732. https://doi.org/10.3390/pr12040732.

[146] Kord K, Bazargan M. Numerical Investigation on J-Shaped Straight-Bladed Darrieus Vertical Axis Wind Turbines Equipped with Gurney Flaps. Int J Energy Res 2024;1:8992210. https://doi.org/10.1155/2024/8992210.

[147] Avalos GM, Hau NR, Quintal-Palomo R, López EO, Gamboa-Marrufo M, Soberanis ME. Aerodynamic techniques to mitigate the 3D loss in the power coefficient of vertical axis wind turbines. Energ Conver Manage 2024;311:118507. https://doi.org/10.1016/j.enconman.2024.118507.

[148] Hassan WU, Jalal A, Bilal MA, Buzal MZ, Asghar H, Ali U. Parametric analysis of a helical-bladed vertical axis wind turbine. Journal of Ocean Engineering and Marine Energy 2024;10(2):383–98. https://doi.org/10.1007/s40722-024-00318-0.

[149] Reddy KU, Deb B, Roy B. Experimental study on influence of aspect ratio and auxiliary blade profile on the performance of H-Type Darrieus wind rotor. Arab J Sci Eng 2024;49(2):1913–29. https://doi.org/10.1007/s13369-023-08049-4.

[150] Pietrykowski K, Kasianantham N, Ravi D, Gęca MJ, Ramakrishnan P, Wendeker M. Sustainable energy development technique of vertical axis wind turbine with variable swept area–An experimental investigation. Appl Energy 2023;329:120262. https://doi.org/10.1016/j.apenergy.2022.120262.

[151] Nimvari ME, Fatahian H, Fatahian E. Performance improvement of a Savonius vertical axis wind turbine using a porous deflector. Energ Conver Manage 2020;220:113062. https://doi.org/10.1016/j.enconman.2020.113062.

[152] Somoano M, Huera-Huarte FJ. Bio-inspired blades with local trailing edge flexibility increase the efficiency of vertical axis wind turbines. Energy Rep 2022;8:3244–50. https://doi.org/10.1016/j.egyr.2022.02.151.

[153] Basker I, Nainangkuppam VM. 3D-CFD flow driven performance analysis of new non-cylindrical helical vertical axis wind turbine for fluctuating urban wind conditions. Energy Sources Part A 2022;44(1):2186–207. https://doi.org/10.1080/15567036.2022.2058654.

[154] Mitchell S, Ogbonna I, Volkov K. Improvement of self-starting capabilities of vertical axis wind turbines with new design of turbine blades. Sustainability 2021;13(7):3854. https://doi.org/10.3390/su13073854.

[155] Chang H, Li D, Zhang R, Wang H, He Y, Zuo Z, et al. Effect of discontinuous biomimetic leading-edge protuberances on the performance of vertical axis wind turbines. Appl Energy 2024;364:123117. https://doi.org/10.1016/j.apenergy.2024.123117.

[156] MacPhee DW, Beyene A. Fluid–structure interaction analysis of a morphing vertical axis wind turbine. J Fluids Struct 2016;60:143–59. https://doi.org/10.1016/j.jfluidstructs.2015.10.010.

[157] Guo W, Gong S, Shen Z, Gong Y, Lu H. Effects of internal rotor parameters on the performance of curved blade-straight blade vertical axis wind turbine. Energ Conver Manage 2024;321:119078. https://doi.org/10.1016/j.enconman.2024.119078.

[158] Syawitri TP, Yao Y, Yao J, Chandra B. Geometry optimisation of vertical axis wind turbine with Gurney flap for performance enhancement at low, medium, and high

ranges of tip speed ratios. Sustainable Energy Technol Assess 2022;49:101779. https://doi.org/10.1016/j.jweia.2024.105853.
[159] Guo J, Zeng P, Lei L. Performance of a straight-bladed vertical axis wind turbine with inclined pitch axes by wind tunnel experiments. Energy 2019;174:553–61. https://doi.org/10.1016/j.energy.2019.02.177.
[160] Guo W, Shen H, Li Y, Feng F, Tagawa K. Wind tunnel tests of the rime icing characteristics of a straight-bladed vertical axis wind turbine. Renew Energy 2021;179:116–32. https://doi.org/10.1016/j.renene.2021.07.033.
[161] Li Y, Tagawa K, Liu W. Performance effects of attachment on blade on a straight-bladed vertical axis wind turbine. Curr Appl Phys 2010;10(2). https://doi.org/10.1016/j.cap.2009.11.072.
[162] Wang WC, Chong WT, Chao TH. Performance analysis of a cross-axis wind turbine from wind tunnel experiments. J Wind Eng Ind Aerodyn 2018;174:312–29. https://doi.org/10.1016/j.jweia.2018.01.023.
[163] Xu YL, Peng YX, Zhan S. Optimal blade pitch function and control device for high-solidity straight-bladed vertical axis wind turbines. Appl Energy 2019;242:1613–25. https://doi.org/10.1016/j.apenergy.2019.03.151.
[164] Sengupta AR, Biswas A, Gupta R. Studies of some high solidity symmetrical and unsymmetrical blade H-Darrieus rotors with respect to starting characteristics, dynamic performances and flow physics in low wind streams. Renew Energy 2016;93:536–47. https://doi.org/10.1016/j.renene.2016.03.029.
[165] Espina-Valdés R, Fernández-Jiménez A, Francos JF, Marigorta EB, Álvarez-Álvarez E. Small cross-flow turbine: Design and testing in high blockage conditions. Energ Conver Manage 2020;213:112863. https://doi.org/10.1016/j.enconman.2020.112863.
[166] Tjahjana DDDP, Arifin Z, Suyitno S, Juwana WE, Prabowo AR, Harsito C. Experimental study of the effect of slotted blades on the Savonius wind turbine performance. Theor Appl Mech Lett 2021;11(3):100249. https://doi.org/10.1016/j.taml.2021.100249.
[167] Kurniawan Y, Tjahjana DDDP, Santoso B. Experimental studies of performance savonius wind turbine with variation layered multiple blade. In IOP Conference Series: Earth and Environmental Science. 2020;541(1):012006. IOP Publishing. https://doi.org/10.1088/1755-1315/541/1/012006.
[168] Sheldahl RE, Blackwell B, Feltz LV. Wind tunnel performance data for two-and three-bucket Savonius rotors. Journal of Energy 1978;2(3):160–4. https://doi.org/10.2514/3.47966.
[169] Santhakumar S, Palanivel I, Venkatasubramanian K. A study on the rotational behaviour of a Savonius Wind turbine in low rise highways during different monsoons. Energy Sustain Dev 2017;40:1–10. https://doi.org/10.1016/j.esd.2017.05.002.
[170] Ahmad M, Shahzad A, Akram F, Ahmad F, Shah SIA. Design optimization of Double-Darrieus hybrid vertical axis wind turbine. Ocean Eng 2022;254:111171. https://doi.org/10.1016/j.oceaneng.2022.111171.
[171] Nagaraju AS, Gupta R, Bhowmik S. Effects of the influence of triangular dimple and aspect ratio on NACA 4412 airfoil on the overall performance of H-Darrieus wind rotor: An experimental investigation. Wind Eng 2024. https://doi.org/10.1177/0309524X241256955.
[172] Xu Z, Dong X, Li K, Zhou Q, Zhao Y. Study of the Self-starting Performance of a Vertical-axis Wind Turbine. Journal of Applied Fluid Mechanics 2024;17(6):1261–76. https://doi.org/10.47176/jafm.17.6.2295.
[173] Kavade RK, Sonekar MM, Choudhari DS, Malwe PD, Sherje NP, Ansari MA, et al. Investigation on fixed pitch Darrieus vertical axis wind turbine. AIP Adv 2024;14(7). https://doi.org/10.1063/5.0203609.
[174] Ghareghani MSM, Abdolahifar A, Karimian S. Numerical investigation on the heliX angle to smoothen aerodynamic torque output of the 3-PB Darrieus vertical axis wind turbine. J Wind Eng Ind Aerod 2023;234:105323. https://doi.org/10.1016/j.jweia.2023.105323.